Morphological Instability of Nanosized Amorphous Silicon Nitride in □-Fe: Diffusional and Elastic Effects

Sylvie Bordère , Hugo Paul Van Landeghem , Abdelkrim Redjaïmia , Mohamed Gouné *

Posted Date: 23 February 2024

doi: 10.20944/preprints202402.1383.v1

Keywords: Nitrogen steels, Amorphous-precipitate, Nitride, Morphological stability, Diffusion, Internal stresses, Modelling, Simulation

Article

Morphological Instability of Nanosized Amorphous Silicon Nitride in α-Fe: Diffusional and Elastic Effects

Sylvie Bordère [1], Hugo Van Landghem [2], A. Redjaïmia [3] and Mohamed Gouné [3,*]

[1] I2M, Univ. Bordeaux, CNRS, UMR 5295, F-33600 Pessac, France
sylvie.bordere@u-bordeaux.fr (S. B.)
[2] SIMaP, Grenoble INP – CNRS – UGA, UMR 5622, 1130 rue de la piscine, BP75, F-38420, St Martin d'Hères, France; hugo.van-landeghem@grenoble-inp.fr (H. V-L.)
[3] Institut Jean Lamour, UMR 7198, CNRS, Universite'de Lorraine, Parc de Saurupt, CS 50840, F-54011 Nancy cedex, France ; Abdelkrim.Redjaimia@univ-lorraine.fr (A. R.)
[4] CNRS, Univ. Bordeaux, Bordeaux INP, ICMCB, UMR 5026, F-33600 Pessac, France
* Correspondence: mm.goune@gmail.com (M.G.);

Abstract: We present a detailed analysis based on both experimental and 3D modeling approaches of the unique silicon nitride precipitation sequence observed in ferritic Fe-Si alloys upon nitriding. At 570°C, Si_3N_4 silicon nitride is shown to form as an amorphous phase into α-Fe ferrite matrix which is morphologically unstable over time. Precipitates nucleate with a spheroidal shape, then develop a cuboidal shape for intermediate sizes and octapod-like morphology for longer time. Using transmission electron microscopy, we show that the transition between spheroid and cuboid morphology depends on particle size and results from competition between interfacial energy and elastic strain energy. The resulting morphology is then shown to be a cuboid shape whose faces are always parallel to the {100} planes of the α-Fe; the <100> directions of the matrix corresponding to the elastically soft directions. There is a critical size of around 45 nm for which the transition between the cuboid shape and the octapod-like morphology takes place. This is characterised by a transformation of quasi-flat facets into concave ones and the development of lobes in the <111> directions of the bcc crystal. To better assess the kinetic effects of diffusion fields and internal stresses on the morphological instability observed, an original 3D model that explicitly couples phase transformations and mechanical fields was developed and applied. The latter, validated on the basis of model cases, is shown to be able to describe the time-evolution of both chemical and mechanical fields and their interactions in diffusive mass transport. Using a model system, it was shown that the concentration field around the precipitates and the internal stresses play opposing roles in the cuboid to octapod-like morphological instability. This work gives some clarification regarding the morphological evolution of amorphous Si_3N_4 precipitates, an important point for controlling the mechanical properties of nitrogen steels.

Keywords: Nitrogen steels; Amorphous-precipitate; Nitride; Morphological stability; Diffusion; Internal stresses; Modelling; Simulation

1. Introduction

The need to improve fuel efficiency and safety has led to a high and growing demand for high-strength steels in the automotive industry. The potential of weight reduction directly depends on mechanical properties improvement, which are in turn controlled by the microstructural features. In that context, the precipitation of amorphous Si_3N_4 into α-Fe has received a growing attention over the last ten years [1–5]. There are several reasons for this interest. On the one hand, the nanometric size and high density of these particles significantly increase the strength of the alloy [6,7]. On the other hand, the amorphous Si_3N_4 has a density half that of iron, imparting a substantial weight saving potential to Si_3N_4-containing steel sheets for automotive applications [6] .

From a more fundamental point of view, the precipitation of Si_3N_4 in α–Fe has very singular characters. (i) The amorphous nature of the precipitates is unusual for nitrides and carbides in steels

 doi:10.20944/preprints202402.1383.v1

and, more generally, for precipitates formed at low temperature in a metal matrix [1, 4]. (ii) These amorphous precipitates are stable over remarkably long treatment durations and, under certain conditions can transform into a crystalline phase of the same composition [5]. (iii) The observed precipitates display a cuboidal shape, which is remarkable since it is usually explained by crystallographic orientation relationships that do not exist here since Si_3N_4 is amorphous [1,4,5]. Indeed, considering solely the interfacial energy would lead to expect a sphere. (iv) The development of uniquely octapod-shaped nanosized amorphous silicon nitride precipitates in a ferrite matrix was observed at 650°C (not at 570°C) [7]. It was explained (but not proved) by the anisotropic growth induced by anisotropic stress field around the developing precipitates after nucleation. We will come back to this point later.

Morphological instabilities are not only fascinating from a scientific point of view, they also play an important role in the evolution of mechanical properties. For example, the transformation of a spherical particle into a cubic particle negatively affects the ductility of the material due to the increase in plastic strain concentration in the particle sharp corners [8,9]. In superalloys, it is also recognised that changes in precipitate morphology during exposure to typical service temperature influence the mechanical properties [10,11]. It is therefore important to gain a better understanding of the phenomena behind morphological instabilities. To this end, a number of studies have been carried out in Ni-based, Ti-Al based, Al-based alloys during ageing [12–21]. For instance, in Ni-based superalloys, sphere-to-cube and cube-to-plate shape transitions were reported together with the so-called "reverse coarsening" corresponding to the splitting of a single cuboidal precipitate into a pair of plates. Another well-known example is the evolution of Al_3Sc precipitates from spheres to cuboids and then to petals [19–20]. Even if it is difficult to summarise all the conclusions of these studies, given their scale, most of the morphological instabilities can be explained on the basis of thermodynamic arguments, taking into account the contributions of interfacial and elastic energies as well as their anisotropies [22,23]. However, kinetic instability phenomena can play an important role. Indeed, as suggested very recently in the case of precipitation of iron-rich precipitates in Cu-Fe-Co alloys, the morphological instability which turns the flat facets into concave ones cannot be understood by means of thermodynamic arguments only [24]. The kinetic instability phenomena linked to diffusional processes necessarily play a significant role in the observed changes.

In this work, we highlight a size-dependent morphological instability that occurs during the pure growth of Si_3N_4 in α-ferrite at 570°C. The precipitates nucleate in the form of spheres and gradually transform into cubes and further, into octapods. To clarify the mechanisms involved, the microstructural evolutions was investigated using Transmission Electron Microscopy (TEM) and 3D modelling able to describe the time-evolution of both chemical and mechanical fields and their interactions. In particular, this work clarifies for the first time the interplay between diffusional processes and local mechanical fields in the morphological instability of amorphous Si_3N_4 precipitates in ferrite during nitriding, an important point for controlling the mechanical properties of nitrogen steels.

2. Materials and Methods

2.1. Processing and nitriding

The systems studied in this work are two binary alloys: Fe-1.5wt%Si and Fe-3.3wt%Si. They were first cast in $\mathbf{60 \times 125 \times 240\ mm^3}$ ingots. They were then hot rolled down to a 3 mm thickness. The hot rolling end temperature was 850 °C. The resulting sheet was cooled at a rate of 30 °C/s down to 580 °C and at 20 °C/s afterwards down to room temperature. Prior to nitriding, samples of $\mathbf{1 \times 10 \times 75\ mm^3}$ were cut from the annealed sheet. They were ground on SiC papers down to P2400-gritbefore being cleaned in an ultrasound cleaner in ethanol. Specimens were annealed so as to obtain an equiaxed ferritic microstructure with an average grain size of roughly 35 μm. They were subsequently nitrided through either gaseous or plasma routes at 570°C for determined durations. After the treatment duration, the plasma was interrupted and the samples were left to return to room temperature at a reduced pressure. During nitriding, nitrogen diffuses into the materials and

 doi:10.20944/preprints202402.1383.v1

combines with alloying elements (here Fe and Si) to form a compound layer on the surface (visible on Figure 1) and a diffusion zone underneath. The latter is of particular interest because it can contain a fine dispersion of silicon nitride, thereby influencing the overall mechanical properties of the material. The matrix is recrystallised and has a bcc structure, as shown by both the micrograph and the X-ray diffraction pattern (see Figure 1).

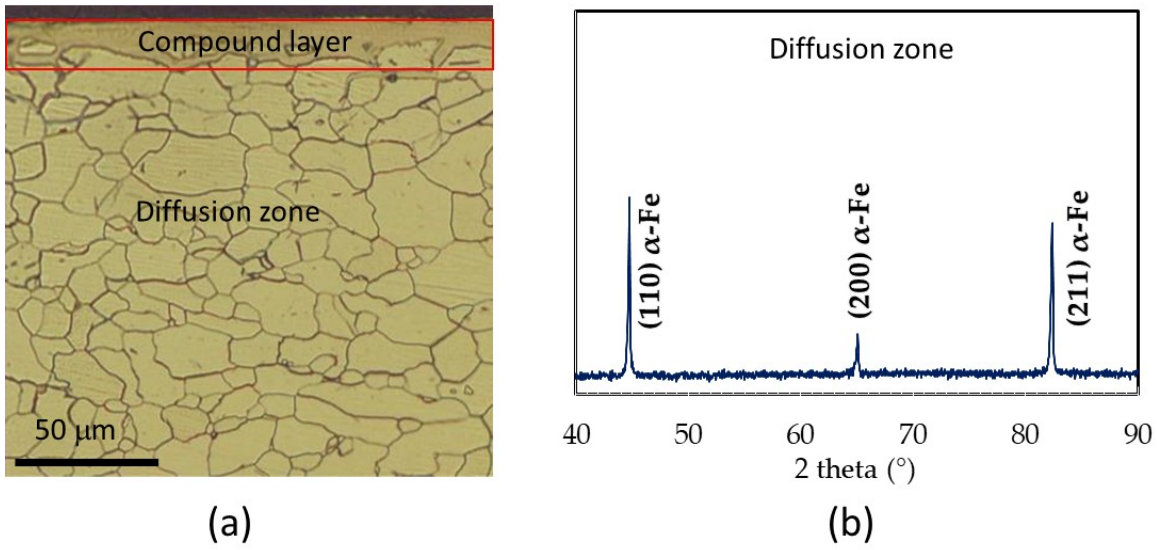

Figure 1. (a) Micrograph obtained after nitriding of the Fe-1.5wt%Si sample at 570 °C for 8 h; (b) Diffraction pattern associated with the diffusion zone.

2.2. Sample characterisation.

The transmission electron microscope observations and analyses were carried out in different ways and using different microscopes. Thin foils were sampled from the specimens by grinding them down to a 60 µm thickness before punching 3 mm discs that were electrolyticly thinned with a Struers Tenupol 5 in a 95 vol.% 2-butoxyethanol/5 vol.% perchloric acid electrolytic bath at 27 V. The resulting thin foils were thoroughly rinsed in ethanol. Replicas were prepared from samples, which were ground and polished down to a 1 µm diamond **fi**nish. They were subsequently etched in Nital 4% for 30 s, rinsed, and dipped in acetone before being laid face down on a biodene **fi**lm. After the acetone dried out, the **fi**lm was peeled off the sample and a thin layer of carbon (several nanometers) was sputtered on it. The **fi**lm was cut in pieces **fi**tting onto standard 3 mm TEM copper grids and dissolved in butan-2-one. Several foils were also prepared via focused ion beam (FIB) milling. Observations of the foils were carried out using two transmission electron microscopes (TEM), a Philips CM200 equipped with an EDAX EDXS as well as a Jeol 2010-F both operated at 200 kV.

The transmission electron microscope observations and analyses were carried out in different ways and using different microscopes. Thin foils were sampled from the specimens by grinding them down to a 60 µm thickness before punching 3 mm discs that were electrolyticly thinned with a Struers Tenupol 5 in a 95 vol.% 2-butoxyethanol/5 vol.% perchloric acid electrolytic bath at 27 V. The resulting thin foils were thoroughly rinsed in ethanol. Replicas were prepared from samples, which were ground and polished down to a 1 µm diamond **fi**nish. They were subsequently etched in Nital 4% for 30 s, rinsed, and dipped in acetone before being laid face down on a biodene **fi**lm. After the acetone dried out, the **fi**lm was peeled off the sample and a thin layer of carbon (several nanometers) was sputtered on it. The **fi**lm was cut in pieces **fi**tting onto standard 3 mm TEM copper grids and dissolved in butan-2-one. Several foils were also prepared via focused ion beam (FIB) milling. Observations of the foils were carried out using two transmission electron microscopes (TEM), a Philips CM200 equipped with an EDAX EDXS as well as a Jeol 2010-F both operated at 200 kV.

3. Modelling

 doi:10.20944/preprints202402.1383.v1

3.1. Methodology

Modelling is a powerful approach to study both the diffusional and the elastic effects on morphological evolution in metallic alloys [23–30]. The dynamic coupling between diffusive phase transformation and mechanical fields remains a difficult task for numerical modelling, since it requires to deal with concentration and pressure jumps at the interface, as well as moving interfaces induced by mass transfers between phases [28–30]. The physical models describing phase transformations, with or without mechano-chemical coupling, can be classified into two main approaches: i) the two-field approaches [31–37], in which the mass transport is resolved within each phase separately, with a condition at the interface for mass conservation which induces the interface movement; ii) the one-field approaches in which mass transport and transfer are modelled by a unique equation for the overall system [38–40]. Phase field modelling belong to the latter since it is based on a free energy functional defined at every point of the multi-phase systems [41–46]. They present great advantages for modelling the evolution of complex 3D microstructures.

From a numerical point of view, there are the Lagrangian methods, which are based on moving grid techniques where the interface is mesh-compliant [31,32,34]. The Lagrangian method has a long tradition in materials science and dates back more than a century to the work of Stefan [47]. It gives an accurate representation of the interface but is difficult to implement because it requires specific reparametrization and constant remeshing throughout the microstructural evolution. This is complicated even further by the topological changes, especially in three dimensions. The Eulerian methods, based on fixed grid, offers a good alternative even if the interface is no longer compliant with the mesh and has to be captured by the evolution of a scalar function in an Eulerian framework. The interface can be tracked by different methods such as the level-set method [37,48], the Volume-Of-Fluid Piece-wise Linear Interface Construction (VOF-PLIC) method [49], the front tracking method [50], or the diffuse interface functions or algebraic Volume-Of-Fluid (VOF) methods [51; 52].

Within that phase transformation modelling field, there are few papers dealing within mechano-chemical coupling of the diffusion mass transport and transfer at the interface mostly based on field phase modelling [24,28–30,33,53].

The problem addressed in the present is a diffusional phase change involving non-isobaric conditions, described in the framework of a binary system (atoms A and B) and two-phase (phases α and β) compounds. The algebraic Volume-Of-Fluid (VOF)-based interface advection method [51] is used to differentiate the two phases and to deal with interface displacement. The methodology is based, for the overall two-phase system, on a single diffusional mass transport equation defined trough an extended chemical potential, described in Equation (1) [40]. This methodology is based on the Darken method [54], readable in [55] in which the intrinsic fluxes of atoms are coupled with a drift velocity (Darken velocity) for mass conservation [56–59]. It was shown that this drift velocity is that of the interface displacement as well, when mass transfers are involved through the interface [40]. The conservation of total momentum is also written using one-field equation described in Equation (2) [60,61]. The mechano-chemical coupling is here achieved through the formulation of the chemical potential, as well as the variation of pressure induced by the phase transformation when the partial molar volumes of the atoms differ from one phase to the other.

3.2. Mass transport equation

The mass transport equation system and transfer at the interface, previously developed for constant pressure and molar volume for A and B within the overall system [40], is here extended to non-isobaric condition and various molar volumes of A and B, which can be highly different from one another, and from a phase to the other. It is defined as:

 doi:10.20944/preprints202402.1383.v1

$$\begin{cases} \frac{\partial c_k}{\partial t} + \mathbf{V}\cdot\nabla c_k = -\nabla\cdot\left(\mathbf{j}_k^d\right) - c_k\nabla\cdot\mathbf{V} \\ with \\ \mathbf{j}_k^d = -c_k\frac{D_k}{RT}\nabla\mu_k \\ \mu_k = \mu_k^* + RT\ ln\left(\frac{x_k}{x_k^*}\right) + \Omega_k(p-p^*)' \\ \mathbf{V} = \mathbf{V}^D + \mathbf{V}^\sigma \\ \mathbf{V}^D = -\sum_{k=A,B}\Omega_k\,\mathbf{j}_k^d \end{cases} \quad (1)$$

where : i) c_k is the concentration of the *k*-species; ii) $\mathbf{j}_k^d$ is the intrinsic diffusion flux of the *k*-species defined within the lattice frame of reference using intrinsic diffusion coefficient D_k of the *k*-atom and the extended chemical potential μ_k; iii) μ_k is defined with the reference potential μ_k^* equals for the two phases at equilibrium, the pure chemical contribution through the term $RT\ ln(x_k/x_k^*)$ (x_k and x_k^* being the atom and the equilibrium atom fractions of the *k*-species, respectively) and the mechanical contribution through the term $\Omega_k(p-p^*)$ (p and p^* being the pressure and reference pressure, respectively); iv) $\mathbf{V}$ is the advection velocity equals for every species and corresponding to the addition of the Darken velocity $\mathbf{V}^D$ and elastic stress relaxation velocity $\mathbf{V}^\sigma$ when mass transfer at the interface induces pressure variation in relation to the molar difference of atoms between the two phases. The Darken velocity is calculated with the intrinsic flux of each species and their molar volume Ω_k. The stress relaxation velocity $\mathbf{V}^\sigma$ is the result of the mechanical governing equation solving Equation (2). For the solving of this diffusion transport equation, Neumann conditions are considered at system boundaries ensuring zero flux at boundaries and thus mass conservation.

3.3. Mechanical governing equation and time derivative of variables

The elastic stress relaxation velocity $\mathbf{V}^\sigma$ can be calculated through the conservation of momentum equation that was developed for fluid/solid or solid/solid systems considering for solids elastic behaviour [60,61]. This equation writes:

$$\rho\left(\frac{\partial\mathbf{V}^\sigma}{\partial t} + (\mathbf{V}^\sigma\cdot\nabla)\mathbf{V}^\sigma\right) = -\nabla p + \nabla\cdot\boldsymbol{\tau}, \quad (2)$$

where $\rho = M_A c_A + M_B c_B$ is the density defined using the molar mass M_A et M_B of the *A* and *B* atoms, respectively; and $\boldsymbol{\tau}$ the elastic shear stress tensor.

The time derivative of pressure is defined as:

$$\frac{\partial p}{dt} + \mathbf{V}^\sigma\nabla p = -\frac{1}{\chi_T}(\nabla\cdot\mathbf{V}^\sigma + \nabla\cdot\mathbf{V}_\Sigma^\sigma), \quad (3)$$

where $\nabla\cdot\mathbf{V}_\Sigma^\sigma$ is an equivalent velocity divergence located at the interface and induced by the molar volume change of the *B*-atoms during its transfer from the α-phase to the β-phase. This divergence is defined as:

$$\nabla\cdot\mathbf{V}_\Sigma^\sigma = -\frac{\partial\phi^D}{dt}\cdot\frac{(\Omega^\beta-\Omega^\alpha)}{\Omega^\alpha}, \quad (4)$$

where the constant χ_T is the isothermal compressibility coefficient which depends on the Young's modulus E_Y and the Poisson coefficient ν through the first and second Lamé's coefficients μ_E and λ_E ($\chi_T = (2\,\mu_E + 3\lambda_E)/3$, with $\mu_E = E_y/\big(2(1+\nu)\big)$ and $\lambda_E = E_Y/(1+\nu)(1-2\nu)$), $d\phi^D/dt$ the variation of the phase function induced by the Darken velocity, Ω^α and Ω^β are the molar volume of both *A* and *B*-atoms in the α and β phases respectively.

The time derivative of the elements of the stress tensor is defined as:

$$\frac{d\tau_{ij}}{dt} = \frac{\partial\tau_{ij}}{\partial t} + \mathbf{V}^\sigma\nabla\tau_{ij} = 2\mu_E\left(\frac{1}{2}(\nabla\mathbf{V}^\sigma + \nabla^t\mathbf{V}^\sigma) - \frac{1}{3}\nabla\cdot(\mathbf{V}^\sigma)\mathbf{I}\right)_{ij}. \quad (5)$$

The displacement of the interface is determined through the advection equation of the phase function ϕ:

$$\frac{\partial\phi}{\partial t} = (\mathbf{V}^D + \mathbf{V}^\sigma)\cdot\nabla\phi = 0. \quad (6)$$

 doi:10.20944/preprints202402.1383.v1

During the simulation, the physical characteristics Y are updated using the phase function ϕ with $\phi = 0$ for the α-phase (matrix) and $\phi = 1$ (particle) for the β-phase, and the P^{α} and P^{β} constant values characterizing the α and β phases, respectively. P is defining either the compressibility coefficient χ_T, the Lamé's coefficient μ_E, the k-species diffusion coefficient D_k, the equilibrium molar fraction of the k-species x_k^* at reference pressure p^* or the molar mass of the k-species M_k.

$$P = (1 - \phi)P^{\alpha} + \phi P^{\beta}. \quad (7)$$

Constant external pressure is considered for solving Equation (2) allowing total elastic strain energy to relax.

3.4. Numerical methodology and discretization

The one-field Equations (1) and (2) are discretized in time and space by explicit/implicit methods, respectively, on a staggered grid [40,61] using the parallel framework of the Notus Computational Fluids Dynamics code [62–65]. A second order centered scheme is used for the discretization of Equation (2) and the diffusion term only in Equation (1) and Equation 2. A Lax-Wendroff scheme with a super bee flux-limiter [51] is used to solve the advection term of Eq. (1, 3, 5, 6). Figure 2 shows the two-phase system discretization and the matrix/precipitate-interface represented by the value of the phase function $\phi = 0.5$.

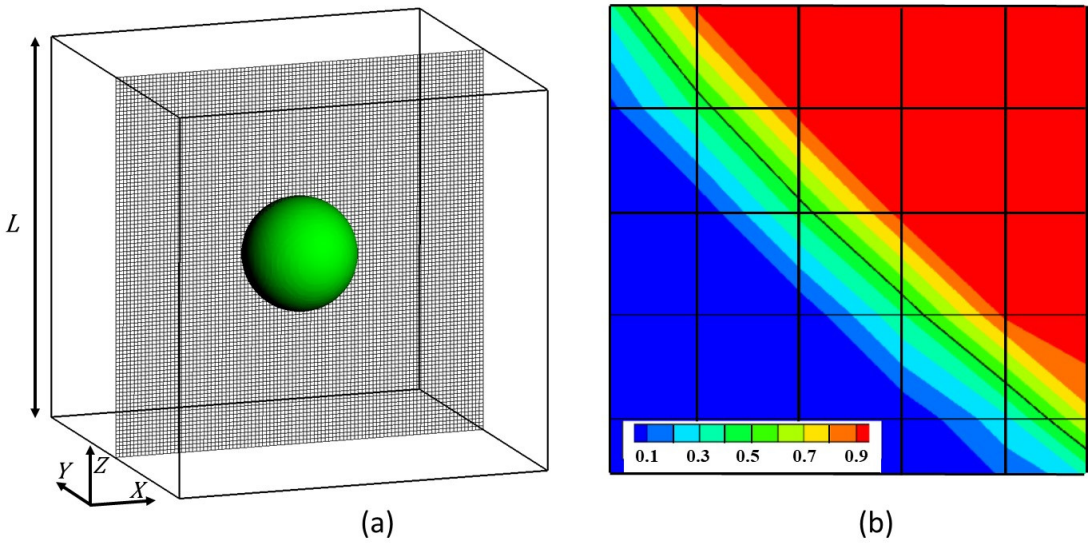

Figure 2. (a) 3D representation of a particle/matrix system into the simulation box of length L and 2D visualization of the mesh grid in the (100)-plane; (b) 2D visualization of the phase function ϕ discriminating the matrix $\phi = 0$ (blue color) from the particle $\phi = 1$(red color). At the interface, the ϕ-function varies continuously. The location of the interface is defined for $\phi = 0.5$ with the full line in black color.

3.5. Modelling validation

3.5.1. Analytical kinetic solutions

The modelling methodology, which aims to deal with mechano-chemical coupling of diffusion mass transport and transfer through the interface is here validated.

The simulation results will thus be compared to the exact solution of the spherical particle growth kinetics developed by Zener [66]. This analytical solution, without any stress field, was completely described in the previous work dealing with the diffusion-controlled phase transformation using the Darken method [40]. For homogeneous β-phase $c_B^{\beta} = c_B^{\beta *}$, assuming Fick's first law for the diffusion of the B-atoms in the α-phase with a constant inter-diffusion coefficient D,

 doi:10.20944/preprints202402.1383.v1

and considering a semi-infinite system insuring zero-flux boundary condition, $c_B^\alpha(x=\infty,t)=c_B^{\alpha 0}$, the growth kinetics of the particle radius r is defined by :

$$r(t)=\kappa\sqrt{4Dt}, \tag{8}$$

where κ is the solution of an equation depending on the coefficient of the supersaturation degree ω. For constant total phase concentration $C^\alpha=C^\alpha=C$, the supersaturation degree is defined by:

$$\omega=\frac{x_B^{\alpha *}-x_B^{\alpha 0}}{x_B^{\alpha *}-x_B^{\beta *\prime}}, \tag{9}$$

where $x_B^{\alpha 0}$ is the initial atom fraction within the α-phase. The stress field induced by a misfitting spherical particle into a matrix will modify, through mechano-chemical coupling, the supersaturation degree ω. To determine ω in the stress field, we first need to know the pressure jump at the interface $(p^\beta-p^\alpha)$ from which it is possible to determine the displacement of the equilibrium atom fraction $x_B^{\alpha\prime}$ at the interface on the α-phase side from the relation :

$$x_B^{\alpha\prime}=x_B^{\alpha *}\exp\left(\frac{\Omega_B(p^\beta-p^\alpha)}{RT}\right), \tag{10}$$

assuming that $\Omega_B^\beta\approx\Omega_B^\alpha=\Omega_B$ for low elastic strain deformation. It is interesting to note that the Equation (10) is identical to the one conventionally used to determine the increase in solubility in the presence of a stress field [67] since both derived from the criterion of equality of chemical potential in the presence of stress field.

To determine the pressure jump at the interface, we decided to use the Sherer's analytical model [68] which, unlike the classical Eshelby model [69], takes into account the interaction of stress fields. So, the misfitting spherical β-precipitate of radius r is placed in a α-matrix. Purely elastic and isotropic behaviour is considered for both phases and the α/β interface is supposed to be perfect. Their Young modulus E_Y^α and E_Y^β and their Poisson coefficients ν^α and ν^β can however be different. For sake of simplicity, the crystallographic modification associated the $\alpha\rightarrow\beta$ transformation of a small volume element is expressed by the following Eigenstrain tensor that corresponds to hydrostatic compression or tension:

$$\boldsymbol{\varepsilon}=\begin{pmatrix}\varepsilon^* & 0 & 0\\ 0 & \varepsilon^* & 0\\ 0 & 0 & \varepsilon^*\end{pmatrix}, \tag{11}$$

where $3\varepsilon^*=\Sigma=-\frac{(\Omega^\beta-\Omega^\alpha)}{\Omega^\alpha}$. The misfittig particle characteristics will be defined in the following by the term Σ. Under these conditions, the author shows [68] that hydrostatic stresses are uniform both in the β-precipitate and α-matrix volumes, whatever the volume fraction of the precipitate f_V. Moreover, for low volume fraction, the level of hydrostatic stress into β-phase is higher than in the α-phase. Furthermore, the β-precipitate is under hydrostatic compression if its molar volume is higher than the one of the α-matrix. Concerning the shear stress field, it is reduced to zero in the precipitate and it is non-uniform in the α-matrix and depends on the distance from the α/β interface. The closer the distance from the α/β interface is, the higher the level of both stresses and strains is.

3.5.2. Simulation results

Two comparative simulations have been performed, one without any stress field and the other with the misfitting particle stress field. For both simulations, shared physical constants are considered: $x_B^{*\alpha}=0.08$; $x_B^{*\beta}=1.0$; $x_B^{0\alpha}=0.1$; $x_B^{0\beta}=1.0$; for low elastic strain deformation $\Omega_B^\beta\approx\Omega_B^\alpha=\Omega_B=7.087\ \mathrm{cm^3.mol^{-1}}$, implying that the total phase concentration $C^\beta\approx C^\alpha=C=1/\Omega_B$ can be assumed constant in the overall system; $M_A=M_B$ = 55.8 g.mol^{-1}; process temperature T = 823 K. The physical constants specific to the case of misfitting particle are: $\Omega_B^\beta=1.0012\,\Omega_B^\alpha$ corresponding to $\Sigma=0.12\ \%$, $E_Y^\alpha=E_Y^\beta=210$ GPa, $\nu^\alpha=\nu^\beta=0$.

The initial configuration for the calculations corresponds to a volume fraction of β-precipitate of $(f_v=0.052\%)$ and a size defined from the dimensionless number $r/L=0.05$; where L is the simulation box length.

 doi:10.20944/preprints202402.1383.v1

The 3D simulation of the misfitting particle shows, in Figure 3, that both the elastic stress and composition fields are isotropic during the beginning of the growth process of precipitate. In that case, both the interfacial concentration and the diffusion flux are shown to be uniform at all points along the precipitate-matrix interface and, consequently, the precipitate morphology remains almost spherical. The characteristics of the hydrostatic and shear stress fields described above, are that expected by the Sherer's model [68] and particularly the uniform pressure field in both particle and matrix volumes (see section 3.5.1).

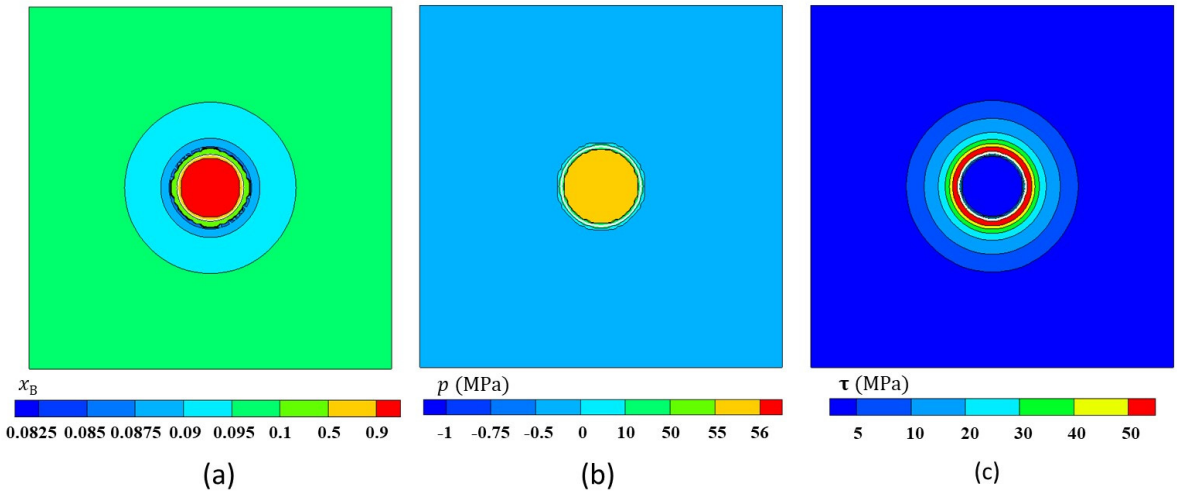

Figure 3. Maps within the three equivalent middle planes $X = 0.5$, $Y = 0.5$, and $Z = 0.5$ at dimensionless time $t \cdot D/L^2 = 0.15$ of: (a) Molar fraction of B-atoms; (b) Pressure. Note that the positive value of pressure corresponds to compressive pressure, whereas negative value corresponds to tensile pressure; (c) Normalized shear stress.

The evolution of hydrostatic stresses in both precipitate and matrix as a function of the particle radius matches very well with the analytical results of Sherer's model [68] as shown in Figure 4. As expected for low particle volume fractions, a relatively high compressive pressure was obtained in the precipitate and a low tensile pressure in the matrix.

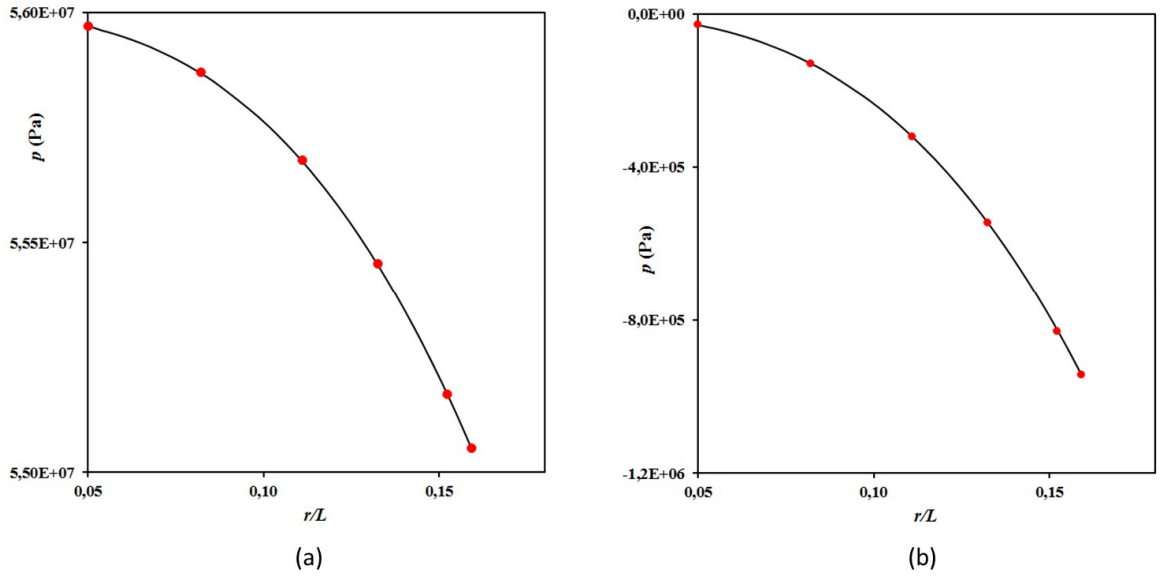

Figure 4. Evolution of the pressure characteristics in the system as a function of the dimensionless particle radius r/L at: (a) The $(X = 0.5, Y = 0.5, Z = 0.5)$-point located in the β-precipitate; (b) The $(X = 0.15, Y = 0.5, Z = 0.5)$-point located in the α-matrix. This evolution is compared for some volume fractions (red dots) to that obtained analytically from the Scherer's model [68].

Preprints.org (www.preprints.org) | NOT PEER-REVIEWED | Posted: 23 February 2024 doi:10.20944/preprints202402.1383.v1

From this result, the pressure jump $(p^{\beta} - p^{\alpha})$ at the interface between the particle and the matrix can be precisely determined. It remains constant during the particle growth and equals to 56 MPa. From Equation (10), the atom fraction displacement at the interface is defined by the value $x_B^{*\prime} = 0.085$. From this value, we can calculate the supersaturation degree ω from Equation (9) to determine the κ-kinetic coefficient in Equation (8) [66]. Table 1 lists the various physical characteristics used to plot the theoretical kinetic law for both the unstressed and stressed configurations.

Table 1. Parameters for the calculation of the kinetic coefficients κ for unstressed and stressed configurations.

	$x_B^{\beta *}$	$x_B^{\alpha *}$	$x_B^{\alpha 0}$	D / L^2 (s^{-1})	ω	κ
Without stress	1.0	0.08	0.01	1.0 x10^{-6}	0.021739	0.1151359
With stress	1.0	0.08	0.01	1.0 x10^{-6}	0.01663	0.0994093

The simulation kinetic results for early times of the precipitation are shown in Figure 5a in the $(r^2/L^2, t.D/L^2)$ dimensionless coordinates.

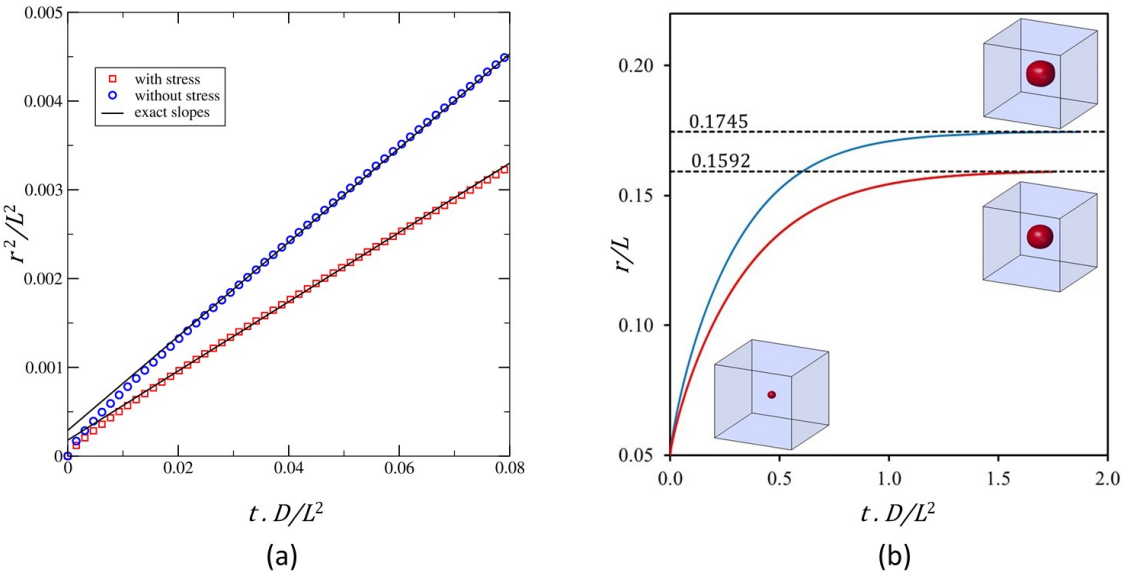

Figure 5. Comparison of the particle growth kinetics. The blue curve and the red curve correspond respectively to the unstressed and stressed cases: (a) Evolution of the square of the dimensionless particle radius as a function of dimensionless time; (b) Evolution of the dimensionless particle radius.The dashed line corresponds to the final equilibrium values.

For both unstressed and stressed systems, the precipitate growth kinetics match well their respective theoretical slopes at the beginning of the transformation as already highlighted in [28,70]. As expected by the theory, the growth kinetics is strongly influenced without changing the classical $t^{1/2}$ temporal power law. The elastic effects decrease both the magnitude of the growth coefficient at early times and the equilibrium radius of the precipitate as shown in Figures 5a and 5b, respectively. The equilibrium particle radius can be determined using the theoretical values of the α-matrix saturation $x_B^{\alpha *}$ and $x_B^{\alpha \prime *}$ for the unstressed and stressed system, respectively (Table 1). The values of $r/L = 0.1745$ and $r/L = 0.1592$ represent the asymptotes to the simulation kinetic curves for long time of the precipitation process. As shown by the profiles of composition given in Figure 6, the elastic field shifts the interface composition closer to the far-field concentration. This tends to decrease the overall growth rate of the precipitate with respect to the unstressed case.

 doi:10.20944/preprints202402.1383.v1

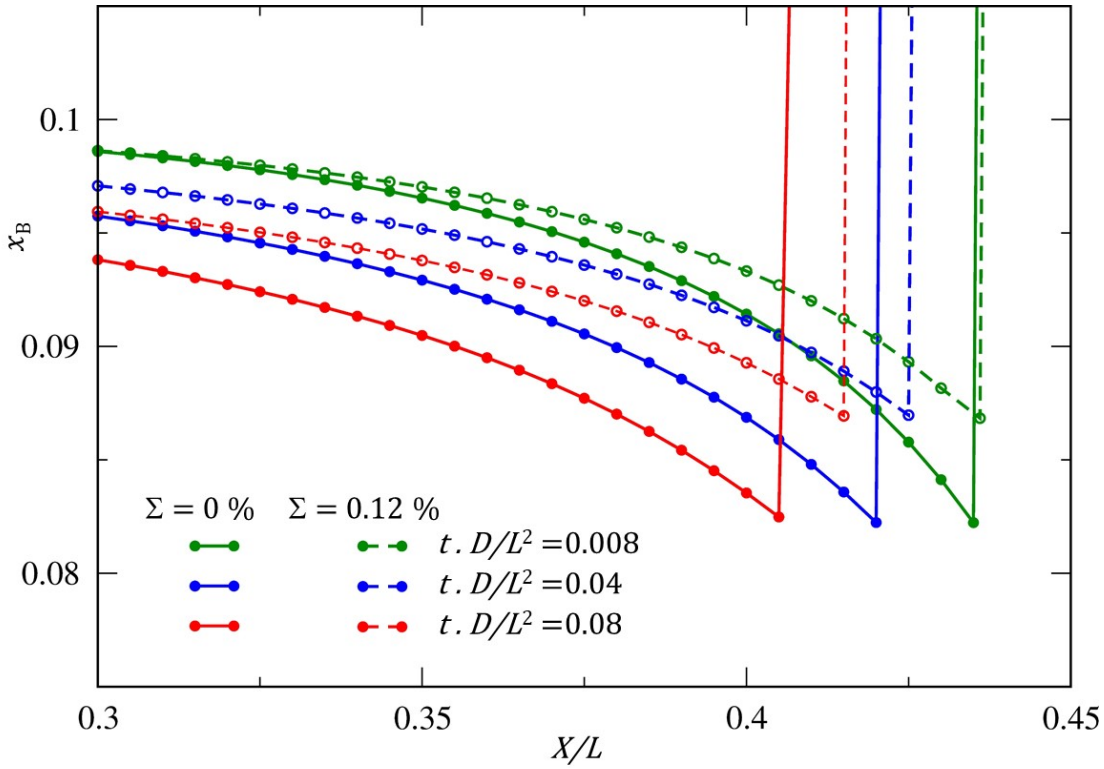

Figure 6. Comparison of the atom fraction profiles of *B*-atoms within the α-phase along the three equivalent middle lines, (*X*/*L*, *Y*/*L* = 0.5, *Z*/*L* = 0.5)-line, (*X*/*L* = 0.5, *Y*/*L*, *Z*/*L* = 0.5)-line and the (*X*/*L*=*0.5*, Y/*L*=0.5, *z*/*L*)-line (*x*/*L*, *y*/*L* = 0.5, *z*/*L* = 0.5)-line during the particle growth. The solid lines and the dashed lines correspond to the unstressed and stressed case, respectively.

4. Results and Discussions

Intense precipitation was revealed on replica bright field TEM images (Figure 7). The precipitates observed were between 15 and 50 nm in size in the Fe-1.5wt% alloy nitrided for 8h. They form homogeneously and heterogeneously on the ferritic grain boundaries. Regions in the proximity of some grain boundaries are found to be free of precipitates. These precipitate free zones (PFZ's) are usually explained by two possible effects. First, precipitates may nucleate first at the grain boundaries (GBs), which are prime nucleation sites, thereby depleting the solute from the adjacent matrix and drastically reducing the driving force for precipitation in this zone. Second, a grain boundary is a sink for vacancies so that regions adjacent to the boundary are unable to nucleate the precipitates, even though the matrix may be supersaturated with solute.

 doi:10.20944/preprints202402.1383.v1

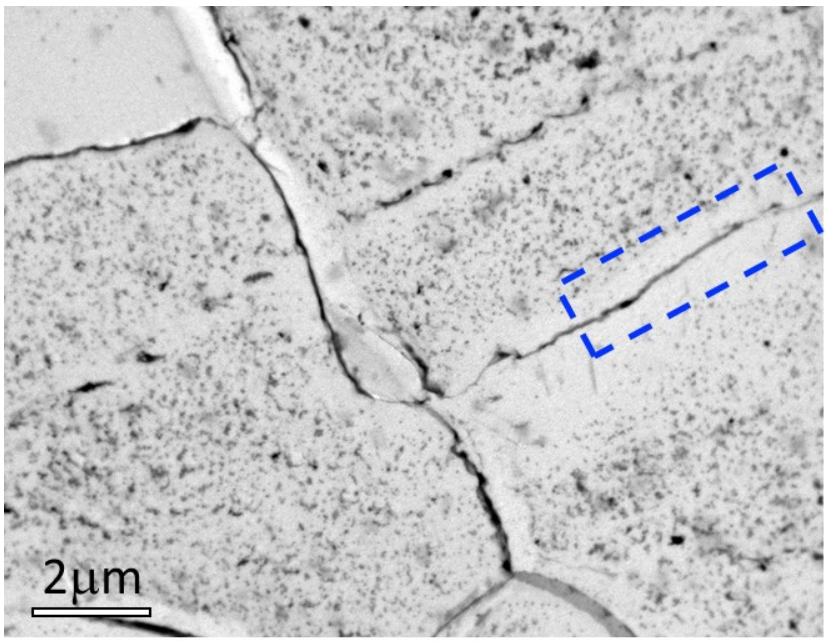

Figure 7. Bright field TEM images of a replica extracted around 50 µm below the surface of the Fe-1.5wt%Si sample nitrided for 8 h. The micrographs show the intense precipitation of silicon nitride particles. It is of interest to note the thin depleted area along the grain boundary as shown in the dotted area.

On a larger scale, the majority of precipitates are cuboid in shape. It is worth noting that the smallest particles adopt a more spheroidal shape (see arrows 1 and 2 in Figure 8a). This point will be detailed later in the paper. The diffraction pattern from an isolated extracted particle and the high-resolution image from a thin foil confirm the amorphous nature of the precipitates (Figure 8b and c). This result is consistent with earlier observations [1,2,4,5]. The composition of these precipitates has also been investigated through various approaches both direct and indirect [1,4,5]. EPMA measurements showed that the average ratio of Si/N was 0.76 ± 0.06 to be compared with the expected 0.75 of stoichiometric Si_3N_4 [1]. Direct electron energy loss spectroscopy (EELS) analyses of the precipitates in the TEM gave a composition of $Si_3N_{3.98\pm0.16}$ [4]. These techniques do, however, raise the question of the precise measurement of nitrogen concentration. Recently, in the same alloys than studied here (Fe-3.5 wt%Si), and using 3D Atom Probe Tomography (3D ATP) we have shown that Si content in silicon nitrides is ~42 at% and N concentration is ~55.5 at%, yielding a Si/N ratio of 0.757 [71]. This ratio is in excellent agreement with the expected 0.75 stoichiometric ratio for Si_3N_4, and suggests that the precipitates deviate little from the Si_3N_4 stoichiometry. All experimental data converge to a Si_3N_4 stoichiometric precipitate in a large range of experimental conditions, which suggests a low tolerance of the phase for deviation from stoichiometry, as is expected for a covalent compound [71]. Based on these experimental pieces of evidence, it will be assumed in the following that the amorphous precipitates are stoichiometric Si_3N_4 silicon nitride.

 doi:10.20944/preprints202402.1383.v1

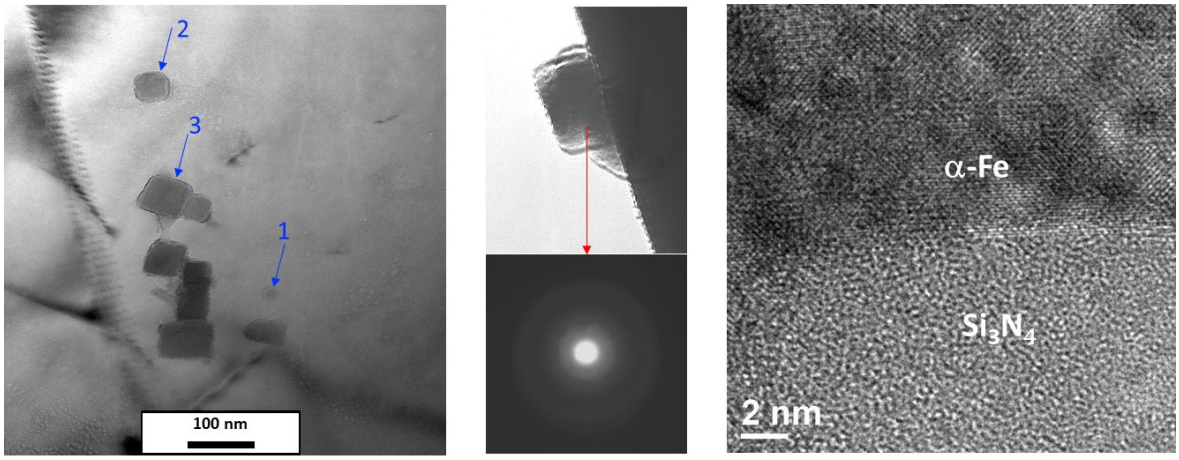

Figure 8. (a) Bright field TEM image at 200kV of a sample of Fe-1.5wt% Si nitrided for 2h at 570°C. The arrows numbered 1, 2 and 3 show that the particles can have a quasi-spherical and/or cuboid morphology; b) Electron diffraction pattern on isolated particle extracted; (c) the contrast observed using high-resolution TEM support the amorphous nature of Si_3N_4.

By positioning the [100] directions of ferrite on a brightfield TEM image taken along the $[001]_{\alpha-Fe}$ zone axis, it was found that all intragranular precipitates having a cuboid shape were systematically oriented with respect to the ferrite matrix (Figure 9) [6]. As it can be seen in Figure 9, the faces of the cuboidal shapes are always parallel to {100} α-Fe planes. Upon closer examination using Scanning Transmission Electron Microscopy (STEM) method (bright field mode), it can be noticed that the shape of the precipitates evolves with their size (Figure 10). At small sizes, the precipitates have a shape that is close to a sphere and as they grow, they turn into cubes with bulging faces. As they grow even further, the faces become concave and the corners of the cuboid develop into lobes, resulting in an ear (or octapod)-like morphology.

 doi:10.20944/preprints202402.1383.v1

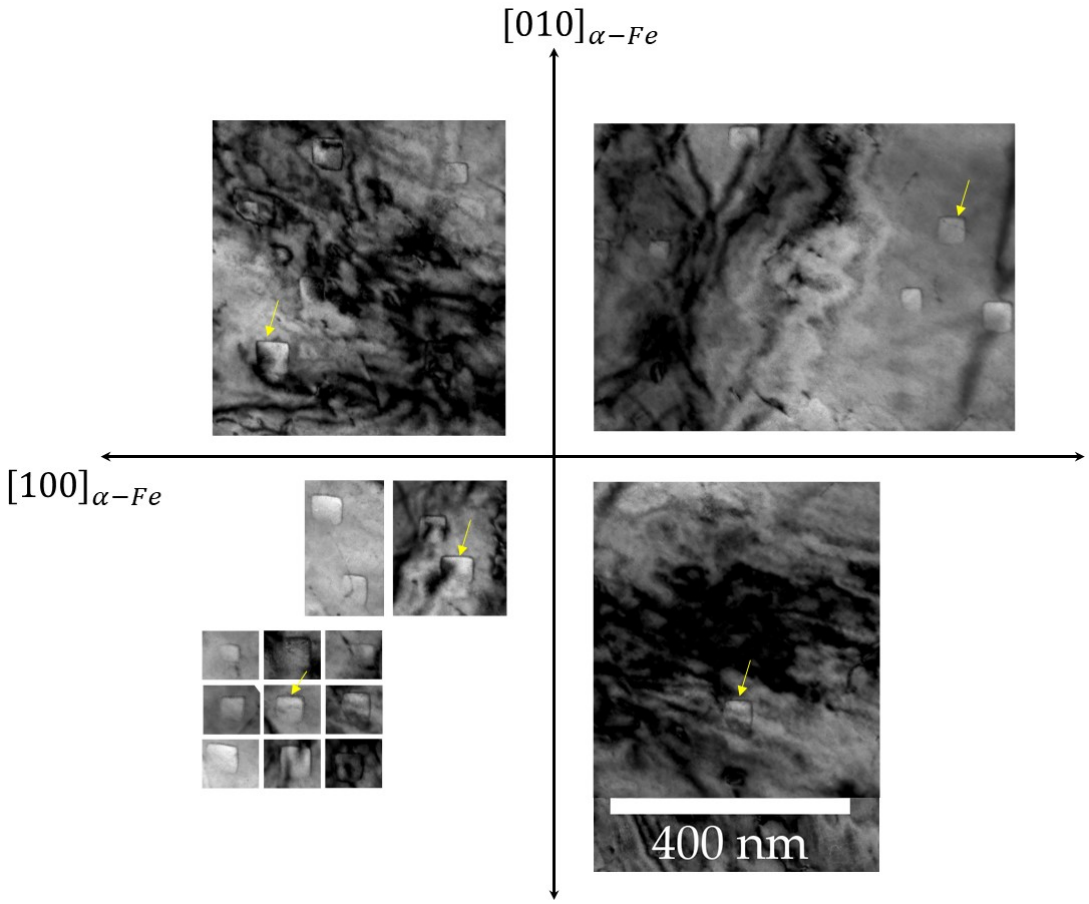

Figure 9. Bright field TEM images of a sample of Fe–1.5wt% Si nitrided for 4 h at 570°C in the $[001]_{\alpha-Fe}$ zone axis. The images were rotated in such a way that the [100] of the ferrite are represented in an orthogonal reference frame. The faces of these cuboids are all systematically parallel to {100} planes of the matrix as indicated by the arrows.

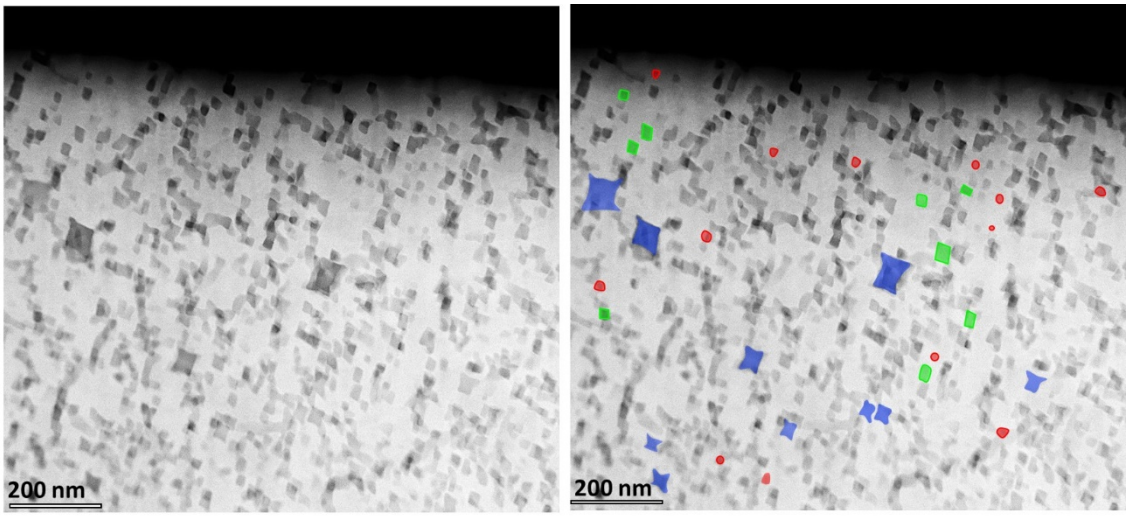

Figure 10. Bright field image of a thin foil prepared using FIB on Fe-3.3wt%Si nitrided for 4h at 570°C. There is a correlation between particle size and morphology. The smallest particles are spheroid-shaped, those of intermediate size are cuboid-shaped, while the largest have concave cuboid-shape with lobes formation at the corners.

We were particularly interested in the morphological instability sequence. Working exclusively on extractive replicas (see an example in the top left insert of Figure 11), the relationship between

 doi:10.20944/preprints202402.1383.v1

equivalent size and morphology was studied for the Fe-1.5wt%Si alloy nitrided for 8h. Several fields covering about 1.5 μm² were analysed and we proceeded step by step. Firstly, the different morphologies observed were classified according to three types: spheroid, cuboid and octapod-like morphology. Next, the average characteristic size of particles with the same morphology was measured; the characteristic size being taken as the diameter for spheroids and the corner to corner distance for cuboids and octapod-like particles. Although subject to inaccuracies in shape and mean size, this method nevertheless allows a semi-quantitative study to be carried out. The morphological instability of precipitates can be further characterised by the non-dimensional length parameter d_1/d_2 yielding the largest length of precipitate along the <111> direction and the smallest length along the <001> direction of the matrix. In the case of spherical particle, $d_1/d_2 = 1$, for cube, $d_1/d_2 = \sqrt{3}$, and $d_1/d_2 > \sqrt{3}$ corresponds to the concave cuboid shape preceding the octapod-like shape of precipitates. This shows that there is a one-to-one link between particle size and particle morphology (Figure 11). For an average characteristic size of less than 25 nm, we found that amorphous Si3N4 particles are spheroid-shaped, for sizes between 25 and 45 nm they are cuboid-shaped and for sizes greater than 45 nm they have an are octapod-like morphology characterised by the formation of lobes at the corners of the particles which can be described as a branching phenomenon (see the sequence shown schematically on the left of Figure 11). It is interesting to note that (i) the cuboid shape observed is characterised by a parameter $d_1/d_2 < \sqrt{3}$, which means here that the corners of the cube are smooth. (ii) for $d_1/d_2 > \sqrt{3}$ we observe the formation of a concave surface on the (100) faces.

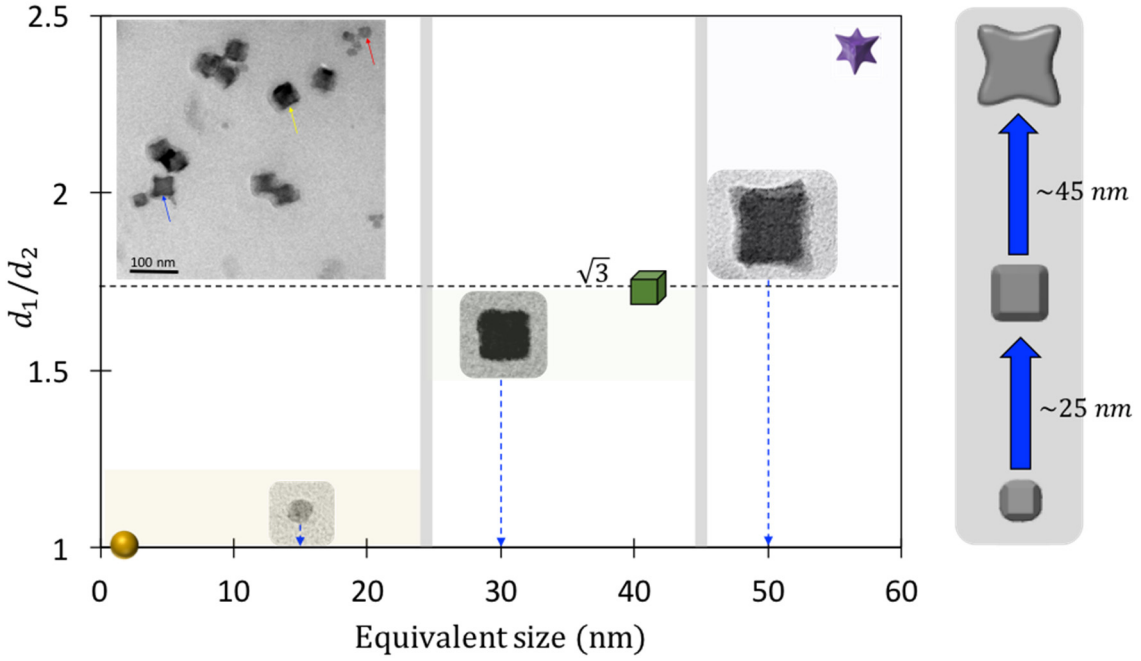

Figure 11. – Relationship between the measured characteristic sizes of amorphous Si_3N_4 precipitates, the dimensionless parameter d_1/d_2 and their observed morphologies in the Fe-1.5wt% nitride for 8 h. $d_1/d_2 = 1$ for a sphere, $d_1/d_2 = \sqrt{3}$ for a cube and $d_1/d_2 > \sqrt{3}$ corresponds to the concave cuboid shape preceding the formation of lobes at the corners of the particles. The inserts at the top-left and in the figure correspond to TEM images obtained on replicas. Morphological instabilities and the corresponding critical sizes are shown schematically on the right of the figure.

To analyse the observations made, it should be noted that, on the one hand, the anisotropy of the interfacial energy between amorphous Si_3N_4 and ferrite is expected to be small, analogous to liquid solid interfaces [72], and consequently, equilibrium shape obtained from the Wulff construction would be close to sphere. On the other, the formation of amorphous Si_3N_4 in the ferrite is accompanied by internal stresses because the two phases have different molar volumes. Consequently, we must consider that the equilibrium shape of precipitates from minimising the sum of the interfacial and the elastic energies at constant volume. The relative contributions of elastic and

 doi:10.20944/preprints202402.1383.v1

interfacial energy to the total energy of the system can be evaluated through the dimensionless parameter λ defined as follow [73,74]:

$$\lambda = \frac{\varepsilon^{*2} C_{44} l}{\gamma}$$

where ε^* is the misfit strain, C_{44} is an elastic constant of the matrix, l is the characteristic size of the precipitates and γ is the surface energy. It is worth noting that the quantity $\varepsilon^{*2} C_{44}$ scales the elastic energy density.

Although this approach can only be applied rigorously under specific conditions (for example same elastic constants for the matrix and the precipitates), it nevertheless provides a simple explanation of our observations on the morphological transition between spheroid and cuboid shapes. For small λ (i. e. small l and/or small elastic energy density), interfacial energy is the dominant factor in setting the equilibrium shape. In this case, the spheroid shape is expected to be stabilised. This corresponds perfectly to our observations, as most Si_3N_4 amorphous particles with a characteristic size of less than 25 nm are spheroid-shaped. Since λ scales linearly with l, it is clear that as the particle increases in size, the effects of the elastic stress on the equilibrium shape become more important. In that case, the spherical particle is no longer in equilibrium. The development of a fourfold anisotropy in the particle shape is then expected, and depends on the elastically hard and soft directions of the matrix [74]. In our case, it is well known that the Young's modulus of the α-Fe matrix phase in the <100> directions are lower than in both the <110> and <111> directions; the <100> directions corresponding to the elastically soft directions [75]. It can be shown in 2D that the high interfacial concentration near the <100> direction results in the flow of mass to the region of the interface near the <110> direction which, is low in concentration [74]. This is expected to produce an increase in curvature along the elastically hard <110> directions and decrease in curvature along the elastically soft <100> directions of the matrix. The resulting morphology would be a cuboid shape that never develops the sharp corners of flat sides characteristic of a cube and whose faces would be always parallel to {100} α-Fe planes. This is in perfect agreement with our observations, as we have shown that all cuboid-shaped Si_3N_4 particles have faces parallel to {100} α-Fe planes (see Figure 9). This work also provides experimental evidences that misfitting particles with nearly isotropic interfacial energy in an elastically anisotropic medium can exhibit some degree of fourfold anisotropy and that the magnitude of the fourfold anisotropy will increase with particle size. The origin of such a phenomenon is mainly linked to the elastic strain energy. However, large λ does not necessarily mean that the misfit must be large, since λ scales linearly with the particle size l. Thus, even particles with small misfits will eventually exhibit the effects of elastic stress for sufficiently large particle sizes.

To better understand the whole sequence of morphological instability, it is now interesting to focus on the transition from cuboid to octapod-like morphology. Observations show that this transition takes place via a transformation of quasi flat-facets into concave ones (see Figures 10 and 11). However, neither the elastic strain energy nor the interfacial energy favour the formation of a concave interface. It is therefore reasonable to suspect that the morphological instability results from kinetic effects. To verify this hypothesis, we propose to evaluate the effects of diffusion fields alone, in the presence and absence of internal stresses, using the 3D model developed. The model system chosen corresponds to an *A-B* binary composed by two phases α and β. The initial state corresponds to a single particle β of cubic shape placed in a matrix α. The initial volume fraction of β is $f_v = 0.1$. The elastic constants used for the simulation correspond to those of ferrite for the α phase and Si_3N_4 for the β phase. These data are given in Table 2.

Table 2. Data used for modelling.

	Symbol	α-phase	β-phase
Initial molar fraction	x_B^0	0.1	1
Equilibrium molar fraction	x_B^*	0.08	1
Young's modulus (GPa)	E_Y	178	320
Poisson coefficient	ν	0.30	0.26

 doi:10.20944/preprints202402.1383.v1

Figure 12 gives the evolution of both the volume fraction f_v and the morphology of a particle β, initially cubic in shape, as a function of the dimensionless time $t \cdot D/L^2$.Firstly, as expected, the growth kinetics is lowered when the misfit between particle and the matrix increases. This is also clearly exhibited on the 3D morphologies obtained at the same dimensionless time $t \cdot D/L^2 = 0.3$ for which the volume fraction of β are higher as the misfit decreases (see points 3, 5, 6 in Figure 12). Secondly, it is clear that the resulting morphology depends on the misfit and therefore on internal stresses. The formation of the octapod-like morphology seems to be favoured in the absence of internal stresses.

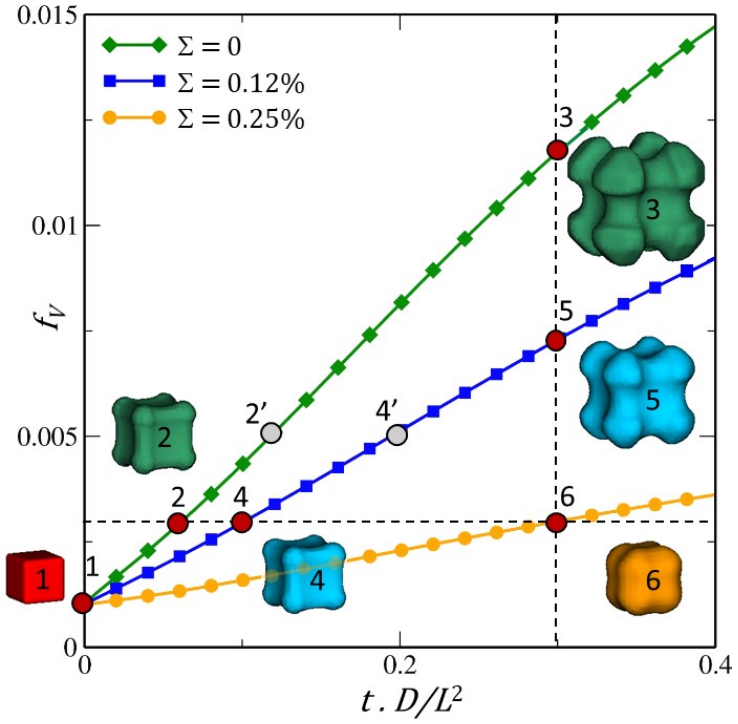

Figure 12. Effect of misfit on the growth kinetics and morphological evolution of the β particle as a function of dimensionless time. Three misfit values, Σ, were considered: 0.25%, 0.12% and 0%. Points 2, 4, 6 and 3, 5, 6 are located on volume iso-fraction $f_v = 0.3\%$ and iso-dimensionless time $t.D/L^2 = 0.3$, respectively. Points 2′ and 4′ correspond to a volume fraction of 0.5% and a misfit of 0.12 % and 0.25 % respectively.

It can be seen that when the driving force for growth is relatively high (3 and 5 in Figure 12), the lobes of the cube appear facetted and, compared with observations, much less pointed in the < 111> directions. This can be explained mainly by the fact that the interfacial and anisotropic effects of diffusion were neglected to better highlight and to decouple the effects of stress and diffusion fields on morphological evolution.

To go further, we consider two different misfit values, $\Sigma = 0\,\%$ $\Sigma = 0.12\%$, and a volume fraction of β of $f_v = 0.5\,\%$ (points 2′ and 4′ in Figure 12). The analysis of the composition and stress fields in a (110) plane of the matrix α shows Figure 13 that : (i) the composition gradient around the particle is less marked in the presence of internal stresses (comparison between Figure 13a-2′ and Figure 13a-4′). This is perfectly consistent with the fact that internal stresses slow down the growth kinetics of β. (ii) Both composition and stress fields are anisotropic (see Figure 13a-4′ and Figure 13b-4′). (iii) in both cases, $\Sigma = 0\,\%$ and $\Sigma = 0.12\%$, we observe the formation of lobes in the corners of the cube, i. e. along the <111> directions of the matrix. The latter can appear well before the diffusion fields overlap (clearly visible in Figure 13a-2′). It is therefore not mainly linked to the interaction between the concentration fields around the particle and the boundaries of the system.

Preprints.org (www.preprints.org) | NOT PEER-REVIEWED | Posted: 23 February 2024 doi:10.20944/preprints202402.1383.v1

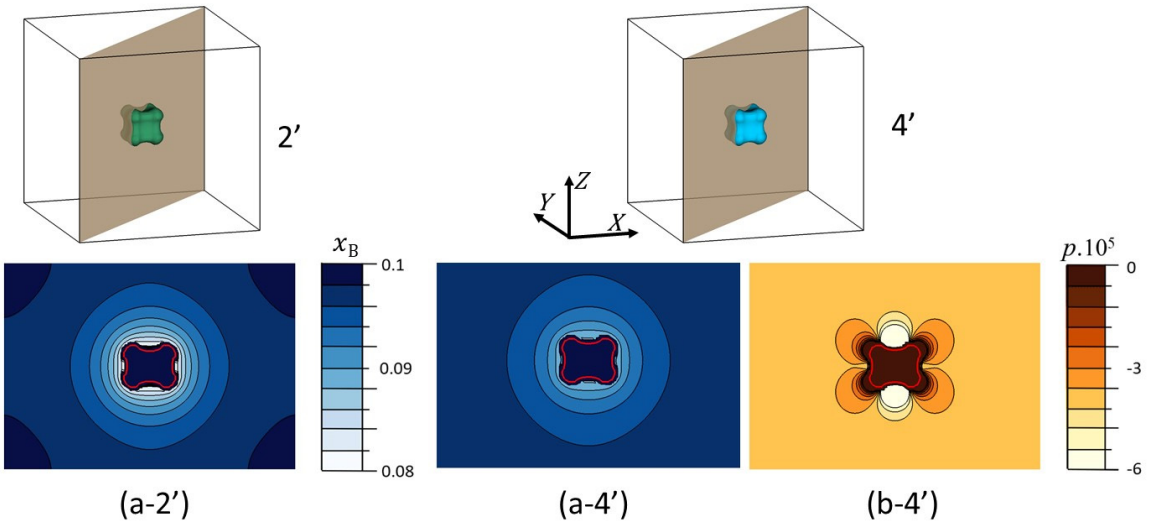

Figure 13. Distribution of both the composition and stress fields in the (110) plane of the matrix α for the two points 2′ and 4′ shown in Figure 12 for $f_v = 0.5\ \%$. The particle β is located inside the red outline. (a-2′) Concentration map of B atoms in the absence of internal stresses ($\Sigma = 0$); (a-4′) Concentration map of B atoms for the misfit $\Sigma = 0.12\%$; (b-4′) Stress field for $\Sigma = 0.12\%$.

These general observations provide an overview of the dynamics of the morphological instability. To refine them, both the concentration and stress profiles were plotted in the <001> and <111> directions of the matrix as a function of the misfit (Figure 14).

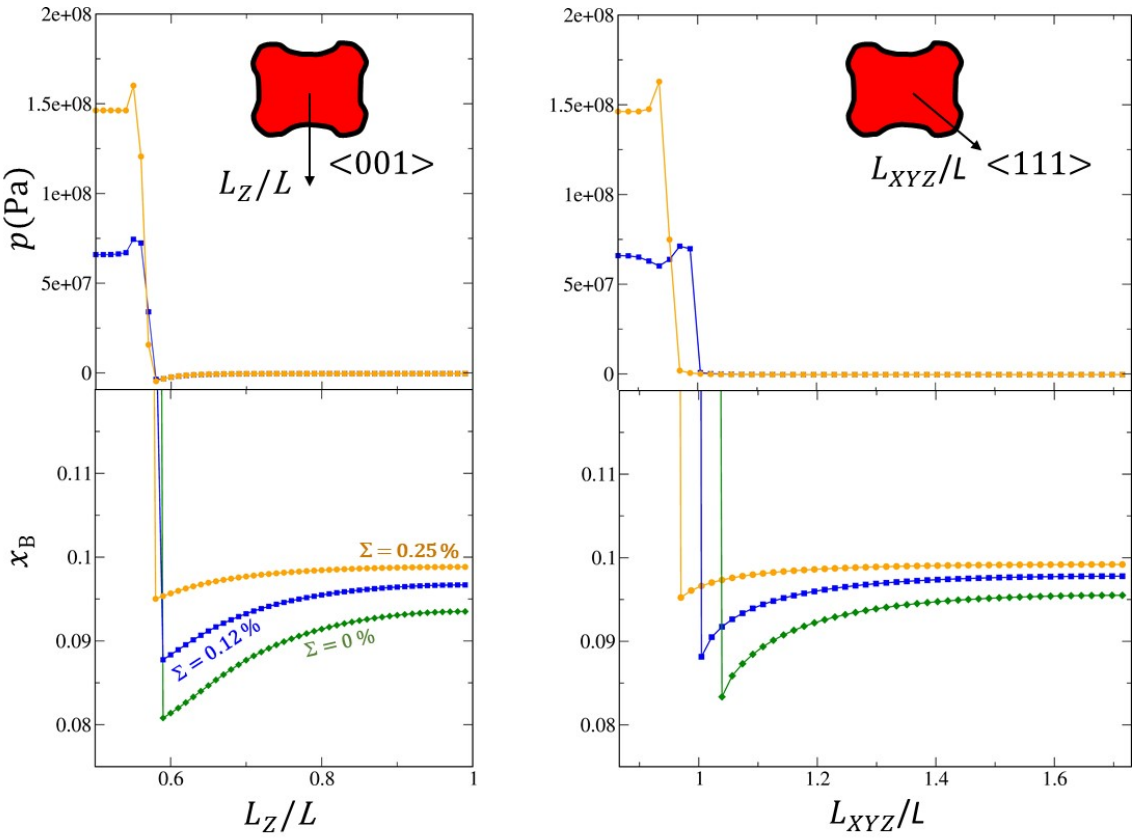

Figure 14. Evolution of the concentration and stress profiles along the <001> and <111> directions of the matrix as a function of misfit ($\Sigma = 0$, $\Sigma = 0.12\%$ and $\Sigma = 0.25\%$). Obviously, the stress profile for $\Sigma = 0$ was not plotted because there are no internal stresses in this case.

 doi:10.20944/preprints202402.1383.v1

The concentration gradients at the α/β interface are a marker of the interface mobility and therefore of the growth rate of β into α. When there are internal stresses (for $\Sigma = 0.12\%$ and $\Sigma = 0.25\%$), particle β is in compression and matrix α in tension. The greater the misfit, the greater the level of stress in the particle β. We clearly show Figure 14 that the concentration gradient in the matrix at the α/β interface is steeper in the <111> direction than in the <001> direction. This explains why the corners of the cuboid grow faster than the faces.

This process has two consequences. Firstly, accelerated growth of the β phase in the <111> directions at the expense of growth in the <001> directions. Secondly, the formation of a concave surface on the faces of the cube. Consequently, the cuboid/octapod-like morphology instability is indeed the result of a kinetic effect induced by the diffusion fields. However, internal stresses play an important role in this instability and, then on morphological evolution. Indeed, we can suspect that the relative growth of β in the <111> and <001> directions depends on the misfit. To confirm this, the evolution of the dimensionless parameter d_1/d_2 yielding the largest length of precipitate along the <111> direction and the smallest length along the <100> direction was plotted as a function of Σ and dimensionless time (Figure 15a). The morphological evolution in the (001) plane of the matrix are given for three dimensionless time 0.1, 0.2 and 0.3 (Figure 15b). Remember that $d_1/d_2 = 1$ and $d_1/d_2 = \sqrt{3}$ correspond to the spherical and cubic shapes respectively, it is clear that diffusion field alone destabilises the cube to octapod-like shape (green curve in Figure 15a and green outline in Figure 15b) because the d_1/d_2 ratio increases as the β particle grows. When the internal stresses increase (i.e., the misfit) we can have two different situations. One in which the d_1/d_2 ratio increases as the particle grows for a misfit of 0.12% (blue curve in Figure 15a). In this case, lobes in the corners of the cube and concavity of the faces of the cube will develop leading to the formation of an octapod-like morphology (blue outline in Figure 15b). However, this process will be kinetically less pronounced than in the absence of internal stresses. The other in which the d_1/d_2 ratio decreases as the particle grows for a misfit of 0.25% (yellow curve in Figure 15a). In that case, the octapod-like morphology is no longer observed. The internal stresses tend to stabilise the cuboid or even to destabilise cuboid to spheroid shape (yellow outline in Figure 15b). The origin of such a phenomenon can be explained from the mechano-chemical potential gradient, which tends to cause the B atoms to diffuse from the most stressed areas (i. e. the regions located in the immediate vicinity of the cuboid corners in the matrix. See Figure 13b-4′) towards the least stressed ones (close to the faces (001). See white zones in Figure Figure 13b-4′). These results were recently confirmed by observations and analysis relating to the morphological transition from cube to petal of the iron-rich particle in the Cu-Fe-Co system formation [24]. Furthermore, it was shown that one of the conditions for branching instability to occur is that elastic driving force should be smaller than the chemical driving to permit growth of the particle corners [76]. This is perfectly consistent with our work.

As a consequence, the morphological instability from cuboid to octapod-like morphology observed is linked to the interaction between the diffusion fields and the stress fields and result of two antagonistic effects. On the one hand, a stabilising effect linked to the internal stresses and, on the other, a destabilising effect linked to the anisotropy of the diffusion fields.

 doi:10.20944/preprints202402.1383.v1

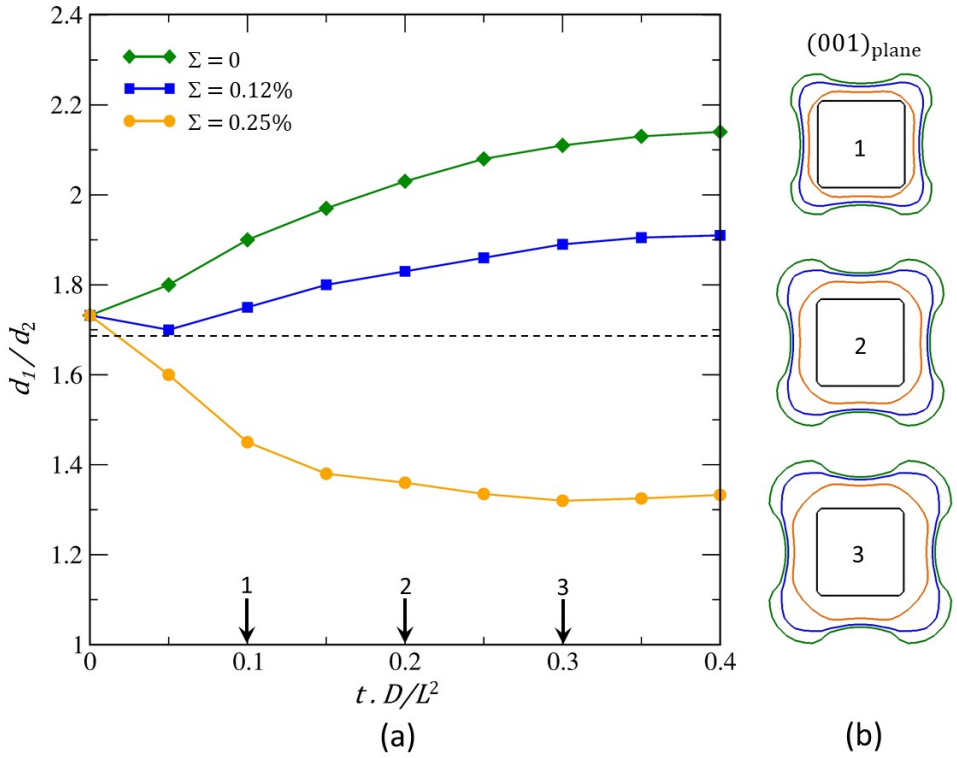

Figure 15. Evolution of: (a) The dimensionless parameter d_1/d_2 yielding the largest length of precipitate along the <111> direction and the smallest length along the <001> direction as a function of misfit and dimensionless time; (b) The morphology of precipitate β as a function of misfit and at three given dimensionless time 0.1, 0.2 and 0.3 in the (001)-plane.

It is interesting to note that the co-formation of crystalline Si_3N_4 and octapod-shaped nanosized amorphous Si_3N_4 precipitates in a ferrite matrix was observed upon nitriding of Fe–4.5 at.%Si alloy for 48h at 650°C [3]. The octapod morphology was attributed to the highly anisotropic stress field around the developing precipitates, which would favour the development of lobes in the <111> directions of the matrix. Our findings show instead that the elastic stress field favours the growth of a cuboid precipitate to the detriment of an octapod one. However, this raises questions regarding the presence of an octapod-like morphology in a system where high internal stresses are expected. In this work it was established that the octapod-like morphology formation is the result of a balance between chemical driving force and elastic driving force. In our experiments, this is observed when the characteristic size of amorphous Si_3N_4 is around 45 nm. This would mean that for particle sizes greater than 45nm, the elastic driving force should be smaller than the chemical driving force. In the case of nitriding, this hypothesis is very realistic for two main reasons. Firstly, the system can be considered as open due to the steady supply of nitrogen atoms from the atmosphere, which enables a large chemical driving force throughout the process [77]. Secondly, in these systems many mechanisms of stress relaxation operate. For example, a local redistribution of nitrogen in specific sites that accommodate stress is possible. This mechanism has already been observed in Fe–N thin films [78] and in Fe–N–Si sputtered films [79]. Interestingly, it was suggested that the presence of the amorphous Si_3N_4 precipitates requires such a stress relaxation mechanism to be operating. Indeed, experimentally, it has been shown that amorphous Si_3N_4 can be destabilized in favour of crystalline α-Si_3N_4 [5] in a low nitrogen activity atmosphere.

4. Conclusion

In this article, we present a detailed analysis on both experimental and 3D modelling approaches of the unique Si_3N_4 precipitation observed in ferritic Fe-Si alloys upon nitriding at 570°C. During growth, the amorphous Si_3N_4 experiences shape instability. First, at early stage of growth, when the

characteristic size of Si_3N_4 is larger than 25 nm, a transition between spheroid and cuboid morphology takes place. Using transmission electron microscopy, we show that it results from competition between interfacial energy and elastic energy. Second, for a critical size of around 45nm, a transition from the cuboid shape to an octapod-like shape was observed. This is characterised by a transformation of quasi-flat facets into concave ones and the development of lobes in the <111> directions of the bcc crystal. Using a 3D original model that couples explicitly phase transformations and mechanical fields, we give some clarifications regarding the role of both diffusional and stress fields on the cuboid to octapod-like morphology instability. The latter is shown to be linked to the interaction between the diffusion fields and the stress fields and results from two antagonistic effects. On the one hand, internal stresses stabilise cuboids while on the other, the anisotropy of the diffusion field promotes an octapod-like shape. The results obtained are in agreement with the experimental observations.

Author Contributions: Conceptualization—S. B, M. G and H. V-L.; Sofware—S. B.; Methodology—S.B, H. V-L and M. G.; Validation— S.B, H. V-L and M. G.; Formal analysis— S.B, H. V-L and M. G.; Investigation H. V-L, A. R.; Data curation—H. V-L, A. R.; Writing—original draft preparation—M. G and S. B.; Writing, Review, and Editing—M. G. and S. B.; Supervision—A. R and M.G.; Project administration—A. R. and M. G.

Acknowledgments: This work was supported by the French State through the program "Investment in the future" operated by the National Research Agency (ANR) and referenced by ANR-11-LABX0008-01 (LabEx DAMAS). The authors gratefully acknowledge support from the METSA network under reference numbers METSA 11 A27 and METSA 11 A44. The authors wish to thank the CC-MEM of the Institut Jean Lamour for their assistance in the electron microscopy work.

References

1. Mittemeijer, E.; Biglari, M.; Böttger, A.; Van der Pers, N.; Sloof, W.; Tichelaar, F. Precipitation of amorphous Si3N4 in α-Fe. *Scripta Mater.* **1999**, *41*, 625-630. https://doi.org/10.1016/S1359-6462(99)00143-8.
2. Meka, S.R.; Jung, K.S.; Bischoff, E.; Mittemeijer, E.J. Unusual precipitation of amorphous silicon nitride upon nitriding Fe–2at.%Si alloy. *Philos. Mag.* **2012**, *92*, 1435-1455. https://doi.org/10.1080/14786435.2011.648226
3. Meka, S.R.; Bischoff, E.; Rheingans, B.; Mittemeijer, E.J. Octapod-shaped, nanosized, amorphous precipitates in a crystalline ferrite matrix. *Philos. Mag. Lett.* **2013**, *93*, 238-245.
4. Van Landeghem, H.P.; Gouné, M.; Epicier, T.; Redjaïmia, A. Unexpected low-temperature crystallization of amorphous silicon nitride into α-Si3N4 in a ferritic Fe–Si matrix. *Scr. Mater.* **2013**, *68*, 187-190. https://doi.org/10.1016/j.scriptamat.2012.10.014.
5. Van Landeghem, H.P.; Gouné, M.; Bordère, S.; Danoix, F.; Redjaïmia, A. Competitive precipitation of amorphous and crystalline silicon nitride in ferrite: Interaction between structure, morphology, and stress relaxation. *Acta Mater.* **2015**, *93*, 218–234. https://doi.org/10.1016/j.matlet.2016.11.064
6. Van Landeghem, H.P.; Gouné, M.; Redjaïmia, A., Investigation of a Ferrite/Silicon Nitride Composite Concept Aimed at Automotive Applications. *Steel Res. Int.* **2012**, *83*, 590-593. https://doi.org/10.1002/srin.201100264
7. Van Landeghem, H.P. Métallurgie à l'azote : Nanoprecipitation amorphe et cristalline de nitrure de silicium dans le système Fe-Si-N. *Thèse de l'Université de Lorraine.* **2012**.
8. Han, S.Z.; Kim, K.H.; Kang, J.; Joh, H.; Kim, S.M.; Ahn1, J.H.; Lee, J.; Lim, S.H.; Han, B. Design of exceptionally strong and conductive Cu alloys beyond the conventional speculation via the interfacial energy-controlled dispersion of γ-Al2O3 nanoparticles. *Sci. Rep.* **2015**, *5*, 17364. https://doi.org/10.1038/srep17364.
9. Böhm, H.J.; Rasool, A. Effects of particle shape on the thermoelastoplastic behavior of particle reinforced composites. *Int. J. Solid Struct.* **2016**, *87*, 90-101. https://doi.org/10.1016/j.ijsolstr.2016.02.028.
10. Nguyen, L.; Shi, R.P.; Wang, Y.Z.; Graef, M.D. Quantification of rafting of ′ precipitates in Ni-based superalloys. *Acta Mater.* **2016**, *103*, 322-333. https://doi.org/10.1016/j.actamat.2015.09.060.
11. Makineni, S.K.; Sugathan, S.; Meher, S.; Banerjee, R.; Bhattacharya, S.; Kumar, S.; Chattopadhyay, K. Enhancing elevated temperature strength of copper containing aluminium alloys by forming L12 Al3Zr precipitates and nucleating ′precipitates on them. *Sci. Rep.* **2017**, *7*, 11154. https://doi.org/10.1038/s41598-017-11540-2

12. Jokisaari, A.M.; Naghavi, S.S.; Wolverton, C.; Voorhees, P.W.; Heinonen, O.G. Predicting the morphologies of γ' precipitates in cobalt-based superalloys. *Acta Mater.* **2017**, *141*, 273-284. https://doi.org/10.1016/J.ACTAMAT.2017.09.003
13. Miyazaki, T.; Imamura, H.; Kozakai, T.; The formation of ′ precipitate doublets in NiAl alloys and their energetic stability. *Mater. Sci. Eng.* **1982**, *54*, 9-15. https://doi.org/10.1016/0025-5416(82)90024-6
14. Doi, M.; Miyazaki, T.; Wakatsuki, T. The effect of elastic interaction energy on the morphology of ′ precipitates in nickel-based alloys. *Mater. Sci. Eng.* **1984**, *67*, 247-253. https://doi.org/10.1016/0025-5416(84)90056-9
15. Doi, M.; Miyazaki, T.; Wakatsuki, T. The effects of elastic interaction energy on the of ′ precipitate morphology of continuously cooled nickel-base alloys. *Mater. Sci. Eng.* **1985**, *74*, 139-145. https://doi.org/10.1016/0025-5416(85)90427-6
16. Doi, M. Coarsening Behaviour of Coherent Precipitates in Elastically Constrained Systems—With Particular Emphasis on Gamma-Prime Precipitates in Nickel-Base Alloys. *Mater. Trans. JIM.* **1992**, *33*, 637-649. https://doi.org/10.2320/matertrans1989.33.637
17. Miyazaki, T.; Imamura, H.; Mori, H.; Kozakal, T. Theoretical and experimental investigations on elastic interactions between ′-precipitates in a Ni-Al alloy. *J. Mater. Sci.* **1981**, *16*, 1197-1203. https://doi.org/10.1007/BF01033832
18. Wang, L.; Zenk, C.; Stark, A.; Felfer, P.; Gabrisch, H.; Göken, M.; Lorenz, U.; Pyczak, F. Morphology evolution of Ti3AlC carbide precipitates in high Nb containing TiAl alloys. *Acta Mater.* **2017**, *137*, 36-44. https://doi.org/10.1016/j.actamat.2017.07.018
19. Marquis, E.A.; Seidman, D.N.; Nanoscale structural evolution of Al3Sc precipitates in Al(Sc) alloys. *Acta Mater.* **2001**, *49*, 1909-1919. https://doi.org/10.1016/S1359-6454(01)00116-1
20. Marsha, E.D.; David, C.D.; David, N.S. Effects of Ti additions on the nanostructure and creep properties of precipitates-strengthened Al-Sc alloys. *Acta Mater.* **2005**, *53*, 4225-4235. https://doi.org/10.1016/j.actamat.2005.05.022
21. Baumann, S.F.; Williams, D.B. Experimental observations on the nucleation and growth of ′(Al3Li) in dilute Al-Li alloys. *Metall. Trans. A* **1985**, *16*, 1203-1211. https://doi.org/10.1007/BF02670325
22. Hazote, A.; Grosdidier, T.; Denis, S. ′ precipitate splitting in Nickel-based superalloys : A 3D finite element analysis. *Scripta Mater.* **1996**, *34*, 601-608.
https://doi.org/10.1016/1359-6462(95)00554-4
23. Grosdidier, T.; Hazotte, A.; Simon, A. Precipitation and dissolution processes in ′ single crystal nickel-based superalloys. *Mater. Sci. Eng. A* **1998**, *256*, 183-196. https://doi.org/10.1016/S0921-5093(98)00795-3
24. Chen, K. X.; Korzhavyi, P. A.; Demange, G.; Zapolsky, H.; Patte, R.; Boisse, J. Morphological instability of iron-rich precipitates in Cu–Fe–Co alloys, *Acta Mater.* **2019**, *163*, 55-67. https://doi.org/10.1016/j.actamat.2018.10.013
25. Diard, O.; Leclerq, S.; Rousselier, G.; Cailletaud, G. Evaluation of finite element based analysis of 3D multicrystalline aggregates plasticity: Application to crystal plasticity model identification and the study of stress and strain fields near grain boundaries. *Int. J. Plasticity.* **2005**, *21*, 691-722. https://doi.org/10.1016/j.ijplas.2004.05.017
26. Musienko, A.; Tatschl, A.; Schmidegg, K.; Kolednik, O.; Pippan, R.; Cailletaux, G. Three-dimensional finite element simulation of a polycrystalline copper specimen. *Acta Mater.* **2007**, *55*, 4121-4136. https://doi.org/10.1016/j.actamat.2007.01.053
27. Durga, A.; Wollants, P.; Moelans, N. A quantitative phase-field model for two-phase elastically inhomogeneous systems. *Comput Mater. Sci.* **2015**, *99*, 81-95. https://doi.org/10.1016/j.commatsci.2014.11.057
28. Ammar, K.; Appolaire, B.; Cailletaud, G.; Feyel, F.; Forest, S. Finite element formulation of a phase field model based on the concept of generalized stresses. *Comput. Mater. Sci.* **2009**, *45*, 800–805. https://doi.org/10.1016/j.commatsci.2008.09.015.
29. Ammar, K.; Appolaire, B.; Cailletaud, G.; Forest, S. Combining phase field approach and homogenization methods for modelling phase transformation in elastoplastic media. *Eur. J. Comput. Mech.* **2009**, *18*, 485-523. https://doi.org/10.1007/s11012-014-0011-1.
30. Cottura, M.; Appolaire, B.; Finel, A.; Le Bouar, Y. Phase field study of acicular growth: Role of elasticity in Widmanstätten structure. *Acta Mater.* **2014**, *72*, 200-210. https://doi.org/10.1016/j.actamat.2014.03.045
31. Pabi, S.K. Computer simulation of the two-phase diffusion-controlled dissolution in the planar finite multilayer couples. *Phys. Status Solidi (a)* **1979**, *51*, 281–289. https://doi.org/10.1002/pssa.2210510133.

32. Illingworth, T.C.; Golosnoy, I.O. Numerical solutions of diffusion-controlled moving boundary problems which conserve solute. *J. Comput. Phys*. **2005**, *209*, 207–225. https://doi.org/10.1016/j.jcp.2005.02.031.
33. Duddu, R.; Chopp, D.L.; Voorhees, P.; Moran, B. Diffusional evolution of precipitates in elastic media using the extended finite element and the level set methods. *J. Comput. Phys*. **2011**, *230*, 1249-1264. https://doi.org/10.1016/j.jcp.2010.11.002.
34. Olaye, O.; Ojo, O.A. Leapfrog/Dufort-Frankel explicit scheme for diffusion-controlled moving interphase boundary problems with variable diffusion coefficient and solute conservation. *Modelling Simul. Mater. Sci. Eng.* **2020**, *28*, 015008. https://doi.org/10.1088/1361-651X/ab58f3.
35. Fleckenstein, S.; Bothe, D.A. Volume-of-fluid-based numerical method for multi-component mass transfer with local volume changes. *J. Comput. Phys*. **2015**, *301*, 35–58. https://doi.org/10.1016/j.jcp.2015.08.011
36. Gennari, G.; Jefferson-Loveday, R.; Pickering, S.J. A phase-change model for diffusion-driven mass transfer problems in incompressible two-phase flows. *Chem. Eng. Sci*. **2022**, 259, 117791. https://doi.org/10.1016/j.ces.2022.117791.
37. Schulz, A.; Wecker, C.; Inguva, V.; Lopatin, A.S.; Kenig, E.Y. A PLIC-based method for species mass transfer at free fluid interfaces. *Chem. Eng. Sci*. **2022**, *251*, 117357. https://doi.org/10.1016/j.ces.2021.11735.
38. Maes, J.; Soulaine, C. A unified single-field Volume-of-Fluid-based formulation for multi-component interfacial transfer with local volume changes. *J. Comput. Phys*. **2020**, *402*, 109024. https://doi.org/10.1016/j.jcp.2019.109024.
39. Zanutto, C.P.; Paladino, E.E.; Evrard, F.; van Wachem, B.; Denner, F. Modeling of interfacial mass transfer based on a single-field formulation and an algebraic VOF method considering non-isothermal systems and large volume changes. *Chem. Eng. Sci*. **2022**, *247*, 116855. https://doi.org/10.1016/j.ces.2021.116855.
40. Bordère, S.; Glockner, S. Numerical modelling of diffusion-controlled phase transformation using the Darken method: Application to the dissolution/precipitation processes in materials. *Comput. Mater. Sci.* **2021**, *186*, 109944. https://doi.org/10.1016/j.commatsci.2020.109944.
41. Chen, L.Q. Phase-Field Models for Microstructure Evolution. *Annu. Rev. Mater. Res.* **2002**, *32*, 113-140. https://doi.org/10.1146/annurev.matsci.32.112001.132041**.**
42. Steinbach, I. Phase-field models in materials science. *Modelling Simul. Mater. Sci. Eng.* **2009**, *17*, 073001. https://doi.org/10.1088/0965-0393/17/7/073001.
43. Kim, S.G.; Kim, W.T.; Suzuki, T. Phase-field model for binary alloys. *Phys. Rev. E* **1999**, *60*, 7186–7197. https://doi.org/10.1103/physreve.60.7186.
44. Van Noorden, T.L.; Eck, C. Phase field approximation of a kinetic moving-boundary problem modelling dissolution and precipitation. *Interfaces Free Bound*. **2011**, 29–55. https://doi.org/10.4171/IFB/247.
45. Böttger, B.; Eiken, J.; Apel, M. Multi-ternary extrapolation scheme for efficient coupling of thermodynamic data to a multi-phase-field model. *Comput. Mater. Sci*. **2015**, *108*, 283–292. https://doi.org/10.1016/j.commatsci.2015.03.003.
46. Yang, C.; Li, S.; Wang, X.; Wang, J.; Huang, H. Phase-field simulation of multi-phase interactions in Fe-C peritectic solidification. *Comput. Mater. Sci*. **2020**, *171*, 109220. https://doi.org/10.1016/j.commatsci.2019.109220.
47. Stefan, J. Über die Theorie der Eisbildung, insbesondere über die Eisbildung im Polarmeere. *J. Ann. Phys. Chem*. **1891**, *42*, 269–286.
48. Balcázar-Arciniega, N.; Antepara, O.; Rigola, J.; Oliva, A. A level-set model for mass transfer in bubbly flows. *Int. J. Heat Mass Transf.* **2019**, *138*, 335–356. https://doi.org/10.1016/j.ijheatmasstransfer.2019.04.008.
49. Bothe, D.; Fleckenstein, S. A Volume-of-Fluid-based method for mass transfer processes at fluid particles. *Chem. Eng. Sci*. **2013**, *101*, 283–302. https://doi.org/10.1016/j.ces.2013.05.029.
50. Darmana, D.; Deen, N.G.; Kuipers,J.A.M. Detailed 3D Modeling of Mass Transfer Processes in Two-Phase Flows with Dynamic Interfaces. *Chem. Eng. Technol*. **2006**, *29*, 1027–1033. https://doi.org/10.1002/ceat.200600156.
51. Hirsch C. *Numerical Computation of Internal and External Flows volume 2: Computational Methods for Inviscid and Viscous Flows*, 1st ed.; John Wiley & Sons, Chichester, England, 1990; pp. 536-552.
52. Ubbink, O.; Issa, R.I. A Method for Capturing Sharp Fluid Interfaces on Arbitrary meshes. *J. Comput. Phys*. **1999**, *153*, 26–50. https://doi.org/10.1006/jcph.1999.6276.
53. Kamachali, R.D.; Schwarze, C.; Lin, M.; M. Diehl, M.; Shanthraj, P.; Prahl, U.; Steinbach, I.; Raabe, D. Numerical Benchmark of Phase-Field Simulations with Elastic Strains: Precipitation in the Presence of

Chemo-Mechanical Coupling. *Comput. Mater. Sci.* **2018**, *155*, 541-553. https://doi.org/10.1016/j.commatsci.2018.09.011.

54. Darken, L. Diffusion, Mobility and Their Interrelation through Free Energy in Binary Metallic Systems. *Trans. AIME* **1948**, *175*, 184–201.
55. Sridhar, S. A Commentary on "Diffusion, Mobility and Their Interrelation through Free Energy in Binary Metallic Systems," L.S. Darken: Trans. AIME, 1948, vol. 175, p. 184ff. *Metall. and Mat Trans A* **2010**, *41*, 543–562. https://doi.org/10.1007/s11661-010-0177-7.
56. Herrnring, J.; Sundman, B.; Klusemann, B. Diffusion-driven microstructure evolution in OpenCalphad. *Comput. Mater. Sci.* **2020**, *175*, 109236. https://doi.org/10.1016/j.commatsci.2019.109236.
57. Ågren, J. Diffusion in phases with several components and sublattices. *J. Phys. Chem. Solids* **1982**, *43*, 421–430. https://doi.org/10.1016/0022-3697(82)90152-4.
58. Andersson, J.; Ågren, J. Models for numerical treatment of multicomponent diffusion in simple phases. *J. Appl. Phys.* **1992**, *72*, 1350–1355. https://doi.org/10.1063/1.351745.
59. Danielewski, M.; Wierzba, B. Thermodynamically consistent bi-velocity mass transport phenomenology. *Acta Mater.* **2010**, *58*, 6717–6727. https://doi.org/10.1016/j.actamat.2010.08.037.
60. Bordère, S.; Caltagirone, J-P. A unifying model for fluid flow and elastic solid deformation: A novel approach for fluid–structure interaction. *J. Fluids. Struct.* **2014**, *51*, 344–353. https://doi.org/10.1016/j.jfluidstructs.2014.09.010.
61. Bordère, S.; Caltagirone, J-P. A multi-physics and multi-time scale approach for modeling fluid–solid interaction and heat transfer. *Comput. Struct.* **2016**, *164*, 38-52. https://doi.org/10.1016/j.compstruc.2015.10.009.
62. Notus CFD Code, available on line: https://notus-cfd.org. (accessed on 2 January 2016)
63. Picot, J.; Glockner S. Reduction of the discretization stencil of direct forcing immersed boundary methods on rectangular cells: The ghost node shifting method. *J. Comput. Phys.* **2018**, *364*, 8–48. https://doi.org/10.1016/j.jcp.2018.02.047.
64. Jost, A.M.D.; Glockner, S.; Erriguible, A. Direct numerical simulations of fluids mixing above mixture critical point. *J. Supercrit. Fluids* **2020**, *165*, 104939. https://doi.org/10.1016/j.supflu.2020.104939.
65. Glockner, S.; Jost, A.M.D.; Erriguible, A. Advanced petascale simulations of the scaling up of mixing limited flow processes for materials synthesis. *Chem. Eng. J.* **2022**, *431*, 133647. https://doi.org/10.1016/j.cej.2021.133647.
66. Zener, C. Theory of Growth of Spherical Precipitates from Solid Solution. *J. of Appl. Phys.* **1949**, *20*, 950–953. https://doi.org/10.1063/1.1698258.
67. Li, J.C-M. Physical chemistry of some microstructural phenomena. *Met. Trans. A* **1978**, *9*, 1353-1380. https://doi.org/10.1007/BF02661808
68. Scherer, G.W. *Relaxation in glass and composites*, 1st ed.; Wiley, New-York, USA, 1986; re-ed; Krieger Pub., Malabar, USA, 1992; 331 p.
69. Eshelby, J.D. The elastic interaction of point defects**.** *Acta Metall* **1955**, *3*, 487-490. https://doi.org/10.1016/0001-6160(55)90140-1
70. Laraia, V.J; Johnson, W.C. Growth of a coherent precipitate from a supersaturated solution. *J. Mater. Res.* **1988**, *3*, 257-266. https://doi.org/10.1557/JMR.1988.0257.
71. Martinavicius, A.; Van Landeghem, H.P.; Danoix, R.; Redjaïmia, A.; Gouné, M.; Danoix, F. Mechanism of Si3N4 precipitation in nitrided Fe-Si alloys: A novel example of particle-stimulated-nucleation. *Mater.Lett.* **2017**, *189*, 25–27. https://doi.org/10.1016/j.matlet.2016.11.064
72. Wang, L.; Hoyt, K.J.; Wang, N.; Provatas, N.; Sinclair, C.W. Controlling solid-liquid interfacial energy anisotropy through the isotropic liquid. *Nat Commun* **2020**, *11*, 724. https://doi.org/10.1038/s41467-020-14530-7.
73. Thompson, M. E.; Su, C. S.; Voorhess, P. W. The equilibrium shape of a misfitting precipitate. *Acta Metal. Mater.* **1994**, *42*, 2107-2122. https://doi.org/10.1016/0956-7151(94)90036-1
74. Voorhess, P. W.; Mc Fadden, G. B.; Johnsson, W. C. On the morphological development of second-phase particles in elastically-stressed solid. *Acta Metal. Mater.* **1992**, *40*, 2979-2992. https://doi.org/10.1016/0956-7151(92)90462-N.

 doi:10.20944/preprints202402.1383.v1

75. Souissi, M.; Numakura, H. Elastic properties of Fe-C and Fe-N martensites. *ISIJ Int.* **2015**, *55,* 1512-1521. https://doi.org/10.2355/isijinternational.55.1512.
76. Wang, Y.; Khachaturyan, A.G. Shape instability during precipitate growth in coherent solids. *Acta Metall. Mater*. **1995**, *43*, 1837-1857. https://doi.org/10.1016/0956-7151(94)00406-8.
77. Van Landeghem, H.P.; Gouné, M.; Redjaïmia, A. Nitride precipitation in compositionally heterogenous alloys: Nucleation, growth and coarsening during nitriding. *J. Cryst. Growth* **2012**, *341*, 53-60. https://doi.org/10.1016/j.jcrysgro.2011.12.056.
78. Gupta, R.; Gupta, A.; Leitenberger, W.; Rüffer, R. Mechanism of stress relaxation in nanocrystalline Fe–N thin films. *Phys. Rev. B* **2012**, *85,* 075401. https://doi.org/10.1103/PhysRevB.85.075401.
79. Uchiyama, K.; O'Handley, R.C.; Lattice strain in sputterdeposited Fe–N–Si films: effects of interstitial mobility. *IEEE Trans. Magn.* **1999**, *35,* 2024–2028. https://doi.org/10.1109/20.764906.